Resonant X-Ray Scattering Studies of Charge Order in Cuprates

Riccardo Comin[1,2,3] and Andrea Damascelli[2,3]

[1]Department of Electrical and Computer Engineering, University of Toronto, Ontario M5S 3G4, Canada; email: r.comin@utoronto.ca

[2]Department of Physics & Astronomy, University of British Columbia, Vancouver, British Columbia V6T 1Z1, Canada; email: damascelli@physics.ubc.ca

[3]Quantum Matter Institute, University of British Columbia, Vancouver, British Columbia V6T 1Z4, Canada

Annu. Rev. Condens. Matter Phys. 2016. 7:369–405

First published online as a Review in Advance on January 14, 2016

The *Annual Review of Condensed Matter Physics* is online at conmatphys.annualreviews.org

This article's doi: 10.1146/annurev-conmatphys-031115-011401

Keywords

charge-density wave, charge order, resonant soft X-ray scattering, high-T_c cuprates, superconductivity

Abstract

X-ray techniques have been used for more than a century to study the atomic and electronic structure in practically any type of material. The advent of correlated electron systems, in particular complex oxides, brought about new scientific challenges and opportunities for the advancement of conventional X-ray methods. In this context, the need for new approaches capable of selectively sensing new forms of orders involving all degrees of freedom—charge, orbital, spin, and lattice—paved the way for the emergence and success of resonant X-ray scattering, which has become an increasingly popular and powerful tool for the study of electronic ordering phenomena in solids. We review the recent resonant X-ray scattering breakthroughs in the copper oxide high-temperature superconductors, in particular regarding the phenomenon of charge order, a broken-symmetry state occurring when valence electrons self-organize into periodic structures. After a brief historical perspective on charge order, we outline the milestones in the development of resonant X-ray scattering as well as the basic theoretical formalism underlying its unique capabilities. The rest of the review focuses on the recent contributions of resonant scattering to the advancements in our description and understanding of charge order. To conclude, we propose a series of present and upcoming challenges and discuss the future outlook for this technique.

1. INTRODUCTION AND BRIEF HISTORICAL SYNOPSIS

AF: antiferromagnetic

HTSC: high-temperature superconductor

YBCO: $YBa_2Cu_3O_{6+x}$

LSCO: $La_{2-x}Sr_xCuO_4$

Transition metal oxides have represented, over the years, a traditional platform for strongly correlated electron physics, which has nowadays become a field of its own, encompassing several classes of compounds with one common denominator: the localized character of the low-energy electronic wave functions (with d or f orbital character) and the corresponding prominence of Coulomb interactions in driving the electronic properties of these materials. In conventional metals or semiconductors, the fermiology is essentially determined by the lowering of the total kinetic energy that becomes possible when a periodic potential supports the delocalization of the local orbitals into extended wave functions with a well-defined momentum and a correspondingly homogeneous distribution of the charge density. In correlated electron systems, the on-site Coulomb repulsion between two electrons in the same d or f orbital can overcome the kinetic energy part of the Hamiltonian, inducing the electronic system to find new ways to lower its total energy, often by spontaneous breaking of the native symmetries of the lattice (translational and/or point group symmetry). This tendency leads to the emergence of a rich variety of symmetry-broken electronic phases and represents a distinctive trademark of strongly correlated systems, spanning across families of compounds with an otherwise very different physical chemisty from a chemical standpoint (1, 2).

Within the extended class of correlated electron systems, copper oxides represent a unique breed, owing to the mixed character of the electronic bands, frustrated by the conflicting interplay between the O-2p states—promoting itinerancy and electron hopping—and the Cu-3d states—which hinder charge fluctuations and are conducive to Mott-Hubbard physics and an insulating, antiferromagnetic (AF) ground state (3). This delicate balance can be tuned and controlled by carrier doping, resulting in a phase diagram of astonishing richness and complexity, which is yet to be fully understood (4). Antiferromagnetism has been long known as the ground state in charge-transfer insulating undoped copper oxides (3), whereas unconventional superconductivity was discovered in 1986 (5). To date, several broken symmetries have been detected in the cuprates, which can be categorized into zero-momentum ($Q = 0$) and finite-momentum ($Q \neq 0$) orders, breaking rotational and/or translational symmetry, respectively. These different types of order can involve both the charge sector (nematic state for $Q = 0$, and charge-density wave for $Q \neq 0$) and the spin sector ($Q = 0$ magnetic order, and spin-density wave or antiferromagnetism with $Q \neq 0$), leading to several proposed forms of intertwined electronic orders (2, 6–14).

1.1. First Observations of Charge Order in Cuprates

In this review, we focus on charge order, which is defined as an electronic phase breaking translational symmetry via a self-organization of the electrons into periodic structures incompatible with the periodicity of the underlying lattice. The denomination of charge order, or equivalently charge-density wave, has over time embraced a broad phenomenology. However, charge order was first discovered in the form of stripe order, whose real-space representation is depicted in **Figure 1*a***. In this ordered state, the doped holes (*dark circles*) are segregated into unidirectional structures that act as boundaries separating undoped domains characterized by AF order. Therefore, stripe order in its generalized meaning is an electronic ground state characterized by a combination of magnetic order and charge order with specific geometrical constraints on the ordering wave vectors.

Historically, the first proof of stripe order came from neutron scattering, a momentum-resolved technique that had been extensively used in the early days of high-temperature superconductors (HTSCs) owing to its excellent energy resolution and large magnetic cross section. The first neutron scattering studies of HTSCs focused on the doping and temperature dependence of AF order in $YBa_2Cu_3O_{6+x}$ (YBCO) (15) and $La_{2-x}Sr_xCuO_4$ (LSCO) (16), which

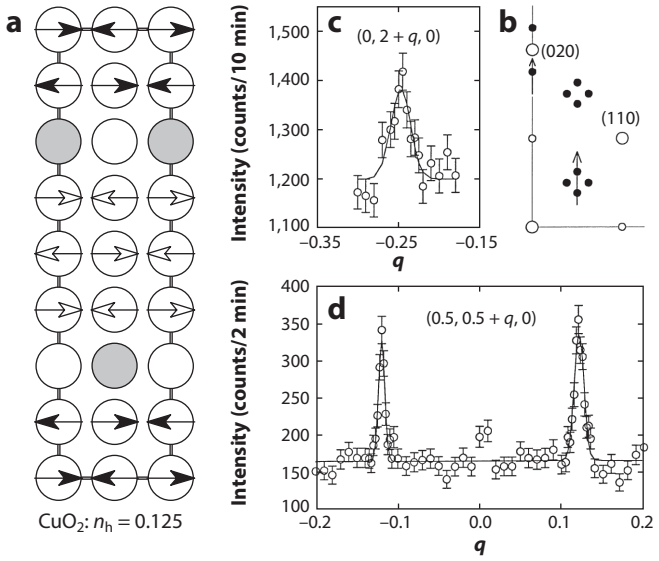

Figure 1

Neutron scattering discovery of stripe order in 12%-doped $La_{1.6-x}Nd_{0.4}Sr_xCu_2O_4$. (*a*) Schematic representation of the stripe pattern: Circles represent the Cu sites in the CuO_2 plane, with arrows denoting the Cu spins and gray circles indicating the location of the doped holes. (*b*) (*HK*0) projection of the reciprocal space showing the location of the measured charge and spin satellites (*black circles*) along the (010) and (110) directions, respectively; white circles represent Bragg reflections. (*c*,*d*) Elastic neutron scattering measurement of the (*c*) charge-order peak at (0, 1.75, 0) and (*d*) magnetic peaks at (0.5, 0.375, 0) and (0.5, 0.625, 0), with scans along the arrows marked in panel *b*. Adapted from Reference 30 with permission.

was determined to be located at wave vectors $\mathbf{Q}_{AF} = (\pm 1/2, \pm 1/2, L)$.[1] Around the same time, the first experimental hint of stripe order was revealed by the independent neutron scattering measurements of Yoshizawa et al. (17) and Birgeneau et al. (18), who reported incommensurate AF modulations in underdoped $La_{1.92}Sr_{0.08}CuO_4$ (8% hole doping) and $La_{1.89}Sr_{0.11}CuO_4$ (11% hole doping), respectively, suggesting the presence of an electronic phase characterized by the quasi-static ordering of the doped holes. A subsequent study by Thurston et al. (19) revealed that the incommensurate AF order could only be found in the superconducting (SC) phase of LSCO [it was later shown to be present also in the insulating phase, albeit with a different modulation vector (20)]. The full momentum structure and doping dependence of incommensurate spin order in LSCO was later uncovered by Cheong et al. (21) and shown to manifest itself as a set of four magnetic peaks at $\mathbf{Q}_{AF-IC} = (1/2 \pm \delta_{IC}, 1/2, L)$ and $\mathbf{Q}_{AF-IC} = (1/2, 1/2 \pm \delta_{IC}, L)$ (see diagram in **Figure 1*b***), with δ_{IC} representing the doping-dependent incommensurability.

The experimental observations from neutron scattering spurred an intense theoretical activity, aimed at addressing two primary phenomenological findings: (*a*) the momentum structure of the incommensurate AF order and its relationship to the ordering of the doped holes, and (*b*) the emergence of incommensurate AF order only within the SC phase, which pointed at an

[1]Hereafter, we use reciprocal lattice units (r.l.u.) for wave vectors in momentum space. Reciprocal lattice units represent a notation where wave vectors are expressed as $\mathbf{Q} = (H, K, L)$, corresponding to $\mathbf{Q} = (H \cdot 2\pi/a, K \cdot 2\pi/b, L \cdot 2\pi/c)$ in physical units (typically, $Å^{-1}$). Also, unless otherwise stated, we refer the wave vectors to the undistorted unit cell, where the **a** and **b** axes (and, correspondingly, the reciprocal axes **H** and **K**) are parallel to the Cu-O bond directions with lattice parameters equal to the nearest Cu-Cu distance.

LNSCO: $La_{2-x-y}Nd_ySr_x$-$CuO_{4+\delta}$

STM: scanning tunneling microscopy

intimate interplay between short-range magnetism and superconductivity in the cuprates. The short-range attractive interaction between segregated charges was initially proposed as a pairing mechanism for the SC state (22), whereas several numerical studies of the Hubbard model near half-filling were performed under different conditions: using mean-field theory without (23, 24) and with (25) charge fluctuations, within Hartree-Fock approximation (26, 27), and using exact diagonalization methods (28). All these studies pointed to a symmetry-broken ground state with short-ranged charge inhomogeneities organized into an ordered pattern of unidirectional charged arrays, segregated away from the magnetic domains and acting as boundaries for the latter (25). The stripe structure with holes condensed along rivers bounding charge-separating AF domains was expected to manifest itself also as a periodic modulation of the charge, with a wave vector twice as long as in the case of the incommensurate AF peaks (23, 25) and tied to the hole concentration ("a counting rule stating that the number of domain line unit cells is equal to the number of carriers"; from Reference 25).

Such a stripe state was found shortly thereafter by Tranquada et al. in the nickelate compound $La_2NiO_{4+\delta}$ (29), as evidenced by the presence of charge[2] and magnetic satellite reflections in neutron scattering at the (collinear) wave vectors $\mathbf{Q}_{\text{charge}} = (H \pm \epsilon, K \pm \epsilon, L)$ and $\mathbf{Q}_{\text{spin}} = (H \pm \epsilon, K \pm \epsilon, L)$, respectively, reflecting the fundamental relationship between the spin and charge ordering incommensurability factors: $\delta_{\text{charge}} = 2\delta_{\text{spin}}$. These two characteristics (collinearity and twofold proportionality of wave vectors) represent the basic conditions for stripe order, as opposed to other geometries (such as checkerboard). The search for static stripe order in the isostructural LSCO cuprate compound was complicated by the necessity for native fourfold symmetry in the CuO_2 planes to be broken in order to accommodate a stripe state. A solution was eventually obtained with the addition of rare earth impurities (Nd and Eu, in place of La), which distorts the lattice in the otherwise square-symmetric CuO_2 planes and provides an inner strain field stabilizing stripe order. Consequently, in 1995, Tranquada et al. (30) used neutron scattering to detect charge- and spin-order peaks in the same sample of underdoped Nd-substituted LSCO, $La_{2-x-y}Nd_ySr_xCu_2O_{4+\delta}$ (LNSCO) at $\mathbf{Q}_{\text{charge}} = (2, 2 \pm 0.25, 0)$ and $\mathbf{Q}_{\text{spin}} = (0.5, 0.5 \pm 0.125, 0)$, as shown in **Figure 1*c*** and ***d***, respectively. This finding confirmed the wave vector relationship already proven in the nickelate compound, namely that $\delta_{\text{charge}} = 0.25 = 2 \cdot 0.125 = 2\delta_{\text{spin}}$, as well as the equivalence between the incommensurability and the doping—with the former amounting to $\sim 1/8 = 0.125$ at the "magical" doping level of 12.5%—which is another signature of stripe order. This work represented the first direct evidence of stripe order in the cuprates and, together with closely following studies using again neutron (31, 32) as well as X-ray (33) scattering, initiated the whole experimental field of charge-ordering phenomena in HTSCs.

For more extended reviews of neutron scattering studies in the cuprates, we refer the reader to References 9 and 34, whereas for a comprehensive discussion of the theoretical works on charge and spin order, we refer the reader to References 6, 7, and 14.

1.2. Imaging Charge Order in Real Space

Toward the end of the 90s, a series of advancements in scanning tunneling microscopy (STM) methods made it possible to obtain atomically resolved maps with spectroscopic information on the energy-dependent local density of states (LDOS) via the measurement of the bias-dependent tip-sample differential tunneling conductance as a function of the spatial coordinate $\mathbf{r}$, $\mathrm{d}I/\mathrm{d}V = g(\mathbf{r}, V) \propto LDOS(\mathbf{r}, E = eV)$. The atomic resolution enabled by STM setups was key to the detection of density modulations with remarkably short correlation lengths, leading the way to

[2] Neutrons can probe charge order indirectly by detecting the associated distortion of the underlying lattice.

a new era in the study of the nanoscale interplay between different electronic orders and of the resulting granular structure in HTSCs.

The new spectroscopic imaging STM (SI-STM) capabilities were soon applied to the study of HTSCs, with the family of choice being that of Bi-based cuprates, owing to the presence of natural cleaving planes yielding extended, atomically flat surfaces that turned out to be ideal for STM studies. The first compound to be studied was $Bi_2Sr_2CaCu_2O_{8+\delta}$ (Bi2212), a layered cuprate with a BiO–SrO–CuO_2–Ca–CuO_2–SrO–BiO stacking of crystallographic planes, characterized by a weak, van der Waals-type bonding between adjacent BiO layers. In 2002, seven years after the original discovery of stripe order in the La-based compounds, the STM investigation of Bi2212 by Hoffman et al. (35) revealed the presence of charge order in yet another cuprate family. The authors studied cleaved surfaces of slightly overdoped Bi2212, and their topographic STM map is shown in **Figure 2*a***. The corresponding differential conductance map over the same field of view, and upon application of a 5-T magnetic field, is depicted in **Figure 2*b***. In the field-induced vortex cores (*darker spots*), where the SC order is suppressed, fourfold, bidirectional modulations of the LDOS can be clearly imaged. This density modulation, with correlation lengths of the order of 30 Å, provided experimental evidence in support of the expectation for a charge instability (36) in the doping range where the field-induced period-8 spin density modulation was discovered in LSCO (37). The emergence of the periodic modulations within the vortex cores further suggested a direct competition between charge order and superconductivity, in analogy to the phenomenology in the La-based cuprates (38).

Bi2212: $Bi_2Sr_2CaCu_2O_{8+\delta}$

Na-CCOC: $Na_xCa_{2-x}CuO_2Cl_2$

Although similar evidence for charge order was found by Howald et al. (39) at low temperature and in the absence of a magnetic field, around the same time the discovery of quasiparticle interference (QPI) (40) in the SC state and below an energy scale of the order of the SC gap underscored the importance of spectroscopic measurements resolving the observed structure as a function of sample-to-tip bias voltage. The energy dependence of the charge order signal in Fourier space was later explored in the STM study by Vershinin et al. on Bi2212 (41) and Hanaguri et al. (42) on Na-doped $Ca_2CuO_2Cl_2$ (Na-CCOC). **Figure 2*c*** shows the reciprocal space chart of Bi2212—obtained by Fourier transforming the differential tunneling conductance map—in the pseudogap state ($T = 100$ K), where QPI effects from SC quasiparticles are not active. The two-dimensional momentum structure of charge order also can be followed as a function of energy (corresponding to the bias between the STM tip and the underlying surface), and **Figure 2*d*** shows a series of line cuts across the charge-ordering wave vector $\mathbf{Q} \sim 0.21$ r.l.u., along the (H0) direction, as a function of energy. A nondispersive charge-order peak (Q) was found to be present across an extended energy range with almost constant amplitude, thereby proving its independence from the energy-dependent features due to QPI. Charge order in highly underdoped ($0.08 < p < 0.12$) Na-CCOC, including non-SC samples, was discovered around the same period and shown to similarly exhibit an energy-independent momentum structure across a broad range of energies in the pseudogap state. Panels *e–g* and *h–j* in **Figure 2** show, respectively, the two-dimensional real- and reciprocal- (Fourier-transformed) maps of the differential tunneling conductance at 8, 24, and 48 mV bias. Distinctive features can be identified in the Fourier transform maps that correspond to near period-4 electronic modulations along the Cu-O bond directions. The energy independence of these features appears evident from the line cuts shown in **Figure 2*k–m***, demonstrating the presence of a broken symmetry driving static electronic modulations affecting all the electronic states over an extended energy range.

The charge-ordered state in Bi2212 and Na-CCOC was later shown by Kohsaka et al. (43) to break down into bond-centered, locally unidirectional domains, as revealed by tunneling asymmetry imaging. These measurements also revealed the prominence of these electronic modulations at large energy scales, of the order of the pseudogap energy; this represents a tendency confirmed

Bi2201: $Bi_{2y}Pb_ySr_{2-z}La_zCuO_{6+\delta}$

in subsequent studies (44, 45). Evidence for charge order in single-layered Bi-based compounds, $Bi_{2-y}Pb_ySr_{2-z}La_zCuO_{6+\delta}$ (Bi2201), was reported in 2008 by Wise et al. (46) over an extended range of dopings, demonstrating that the charge-order wave vector evolution is compatible with a possible instability arising from the antinodal region of the Fermi surface. A similar doping dependence was also detected in Bi2212 (47–49). In recent years, a possible connection between charge order and the pseudogap state has been unveiled in Bi2212 using high-temperature STM to correlate the onset of the electronic signal from incipient stripes with the pseudogap temperature T^* (50, 51). These findings were followed by temperature-dependent measurements that show a competition between charge order and superconductivity near the Fermi energy (49). Even more recently, the zero-temperature density-wave order was shown to disappear in the vicinity of a putative quantum critical point located at a doping of $p \sim 0.16$ for Bi2201 (52, 53) and $p \sim 0.19$ for Bi2212 (54). Throughout the years, STM and SI-STM provided a constant stream of scientific results and valuable insights on the existence, nature, symmetry, and nanoscale structure of charge order in underdoped cuprates; many of these studies have now been covered by several reviews (55–57).

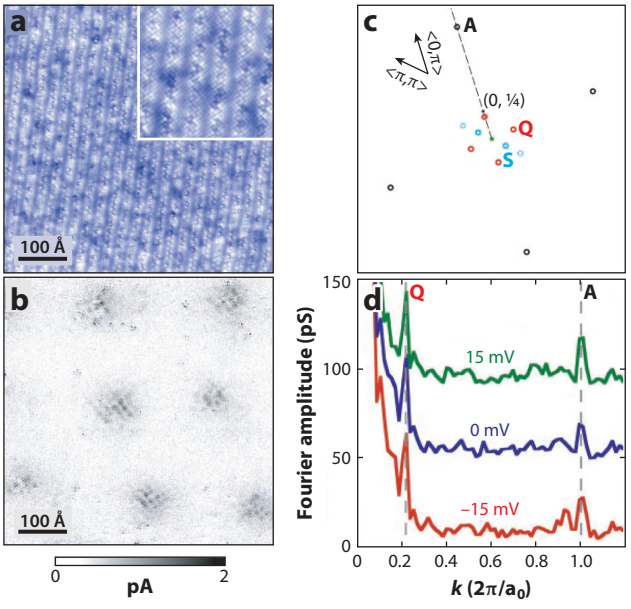

Figure 2

Scanning tunneling microscopy (STM) explorations of charge order in Bi-based cuprates. (*a*) Low-temperature topographic map of a cleaved surface of slightly overdoped ($T_c = 89$ K) $Bi_2Sr_2CaCu_2O_{8+\delta}$ (Bi2212). (*b*) Differential tunneling conductance (dI/dV) map (integrated between 1 and 12 meV) between an applied magnetic field of 5 and 0 T, showing the appearance of period-4 density modulations within the magnetic vortex cores, and over the same spatial region of panel *a*. Adapted from Reference 35 with permission. (*c*) Momentum space representation of the periodic structures observed using STM on Bi2212, including the Fourier peaks from the atomic lattice (A) and the structural supermodulation (S), as well as the charge-order peaks (Q) at $\mathbf{Q} \sim (\pm 0.21, 0)$ and $\mathbf{Q} \sim (0, \pm 0.21)$, in reciprocal lattice units (r.l.u.). (*d*) Energy-resolved Fourier-transformed conductance map along the (10) direction, showing no dependence of the charge-order peak position (Q) on energy, thereby demonstrating the independence of this phenomenon from quasiparticle interference effects. Adapted from Reference 41 with permission. (*e–g*) (*Panels continued on next page*) Conductance maps in Na-doped $Ca_2CuO_2Cl_2$ at different bias voltages, and (*h–j*) corresponding 2D Fourier transforms whose line cuts (*k–m*) along the Cu-O bond directions show the charge-order spatial frequencies and the lack of energy dispersion in the momentum-resolved structures. Adapted from Reference 42 with permission.

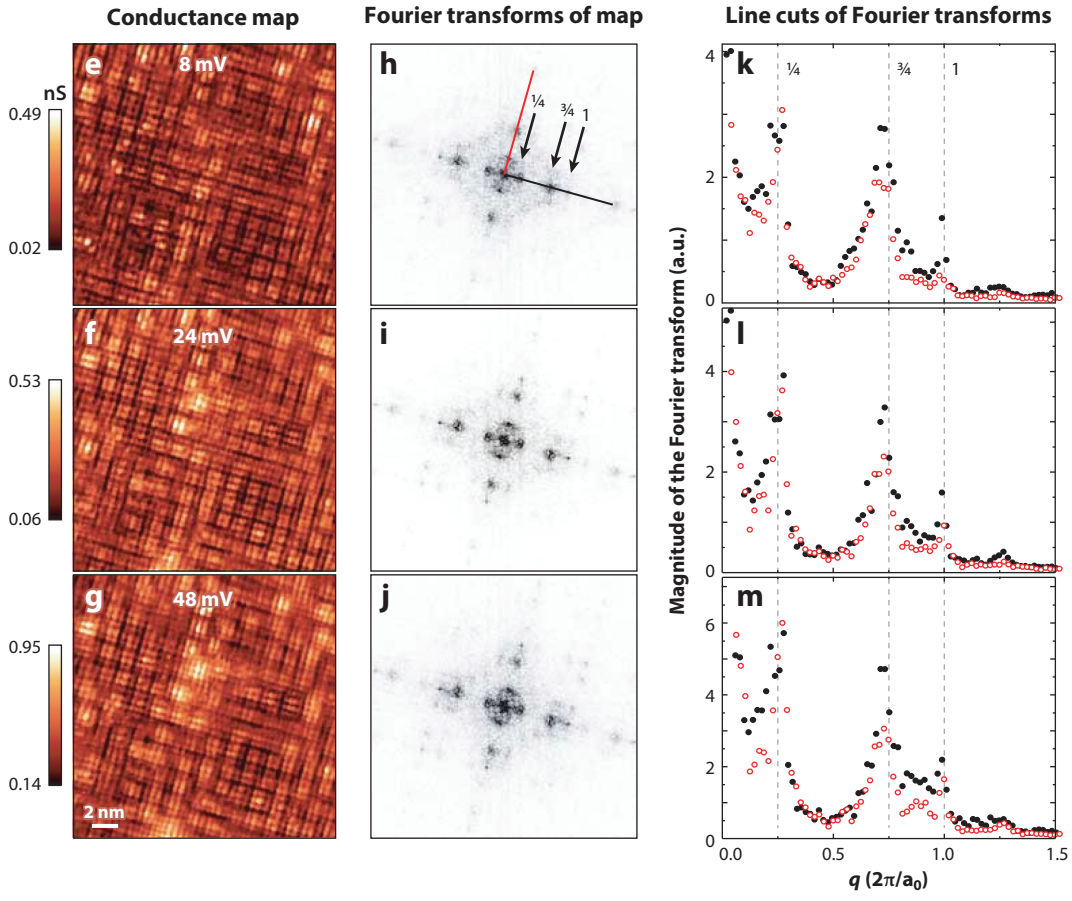

Figure 2

(*Continued*)

2. RESONANT X-RAY METHODS

2.1. Resonant X-Ray Scattering in a Nutshell

X-rays have long been used to investigate the inner structure of matter, thanks to the interaction of light with the electronic clouds surrounding the atomic nuclei (58). The role of photon energy in X-ray scattering has traditionally been marginal—with the exception of anomalous X-ray diffraction, a technique that relies on the strongly varying X-ray absorption near the absorption edges of certain elements to simplify the phase retrieval problem in crystallography and provide a full reconstruction of the atomic positions in complex macromolecular systems (59). The first glimpses of resonant X-ray effects were revealed at the beginning of the 1970s, when de Bergevin & Brunel (60) demonstrated that X-rays are also sensitive to the distribution of electronic spins in magnetic materials by detecting AF Bragg reflections in NiO, thus confirming theoretical predictions by Platzman & Tzoar (61). Following these seminal findings, synchrotron-based X-ray magnetic scattering has been subsequently used as a powerful alternative to neutron scattering on several magnetically ordered systems (62–67); around the same time, the foundations for a comprehensive theory of resonant X-ray scattering (RXS) were laid by Blume and coworkers (68–70). Since its

RXS: resonant X-ray scattering

inception during the 1980s, resonant hard X-ray scattering has developed into an extremely versatile tool (71, 72) for the selective study of ordering phenomena involving the charge, spin, orbital, and lattice degrees of freedom, often offering a unique perspective on their respective interplay.

Historically, hard X-ray methods have anticipated soft X-ray methods owing to the $(\hbar\omega)^3$ dependence of the X-ray attenuation length on photon energy $\hbar\omega$ (ω is the angular frequency of the radiation field), which eliminates the need for vacuum-based experimental chambers for energies $\hbar\omega \gtrsim 5$ keV.[3] Soft X-ray absorption spectroscopy (XAS) was first pioneered using conventional X-ray sources in a transmission geometry on thin films of rare earth metals and oxides, which are known for the large absorption cross section and rich multiplet structure characterizing the $M_{4,5}$ edges ($3d \rightarrow 4f$ transitions) (75, 76). Important advancements in XAS came with the use of synchrotron facilities (77), which produced a higher X-ray flux and further enabled the control of linear and circular X-ray polarization, making it possible to detect magnetic X-ray dichroism effects (78). In the same years, improved detection schemes were being progressively adopted, such as partial electron yield (79), total electron yield (80, 81), and fluorescence yield (82, 83).

The successes of resonant hard X-ray scattering spurred the development of soft X-ray scattering instruments and methods, which presented clear benefits, such as access to the degrees of freedom controlling the electronic structure in transition metal and rare earth oxides, greater sensitivity to surface and interface effects, and native control of incoming light polarization, but also inherent complications, e.g., limited accessible reciprocal space (and a consequent lower boundary of ~3 Å on the smallest measurable periodicity, at ~2 keV), the incompatibility with crystal-based energy or polarization analyzers, and the need for a high vacuum environment. The rise of resonant soft X-ray scattering required special diffractometers capable of simultaneous, in-vacuum control of the sample and detector angles. The first concept of a two-circle diffractometer (with independent sample and detector rotations in the scattering plane) was already pioneered in the late 1980s (84), and further advancements were realized throughout the 1990s and early 2000s at different facilities, including Brookhaven National Lab (85, 86), Laboratoire pour l'Utilisation du Rayonnement Electromagntique (LURE) (87), the Synchrotron Radiation Center (88), the European Synchrotron Radiation Facility (89), the Daresbury Laboratory (90–92), the Berlin Electron Storage Ring Society for Synchrotron Radiation (BESSY) (93), the Swiss Light Source (94), and the Canadian Light Source (95). Motivated by the new insights produced by early resonant inelastic X-ray scattering (RIXS) studies at the Cu-K edge (~8.9 keV) (96–99), the first resonant scattering measurements on cuprates in the soft X-ray regime were performed in 2002 by Abbamonte et al. (100) on thin films of oxygen-doped La_2CuO_4 at the O-K edge ($1s \rightarrow 2p$, $\hbar\omega \sim 530{-}550$ eV) and the Cu-$L_{3,2}$ edge ($2p \rightarrow 3d$, $\hbar\omega \sim 920{-}960$ eV). The sensitivity of these two absorption edges to the doped holes in cuprates had been demonstrated previously (81, 101–103), in particular through the identification of a mobile carrier peak (MCP) structure at $\hbar\omega \sim 528$ eV, i.e., below the onset of the main O-K edge, representing transitions onto the doped hole electronic states with large spectral weight on the O-$2p$ orbitals within the CuO_2 planes. The study by Abbamonte et al. explored momentum space in the ranges $(0, 0, 0.21) - (0, 0, 1.21)$ (orthogonal to the CuO_2 planes) and $(0, 0, 0.6) - (0.3, 0, 0.6)$ (parallel to the CuO_2 planes), and

[3] For example, the attenuation length for X-rays propagating in atmosphere at 10 keV (1 keV) is ~3 m (3 mm) and, as a result, the loss in X-ray flux over 1 m (representing the typical dimension of a scattering diffractometer) is ~30% (100%). Due to the continuous, power-law dependence of X-ray absorption on the photon energy, no precise cutoff can be defined for soft X-rays. However, conventional Cr-K_α X-ray sources exist that operate in air at ~5.4 keV, albeit requiring reduced source-to-sample and sample-to-detector distances. In addition, we note that hard X-ray beamlines still use vacuum conditions along the long pipes transporting the photons from the storage ring to the experimental chamber and from the chamber to the photon detectors.

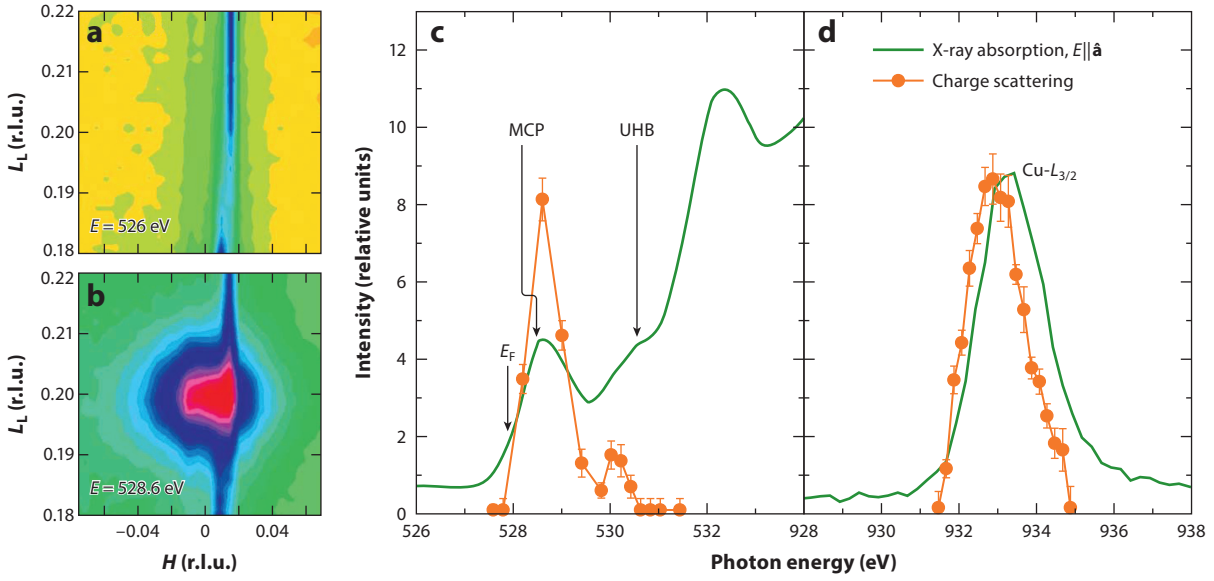

Figure 3

The first soft resonant X-ray scattering (RXS) studies of charge order in cuprates. (*a*,*b*) Reciprocal space mapping of the (*H*0*L*) plane in the nonsuperconducting cuprate compound $Sr_{14}Cu_{24}O_{41}$ measured using soft RXS (*a*) off-resonance (526 eV) and (*b*) at the main absorption peak for doped O-2*p* holes (528.6 eV, corresponding to the $1s \rightarrow 2p$ transition). At resonance (*b*), a superlattice peak is revealed at $\mathbf{Q} = (0, 0, 0.2)$, signaling the crystallization of O-2*p* holes into a static and periodic pattern (Wigner crystal). Adapted from Reference 73 with permission. (*c*) Soft RXS measurements of the stripe-order peak of $La_{1.875}Ba_{0.125}CuO_4$ [located at $\mathbf{Q} \sim (0, 25, 0, 1.5)$] across the O-*K* edge ($1s \rightarrow 2p$), with the X-ray transitions into the mobile carrier states (mobile carrier peak, MCP) and upper Hubbard band (UHB). (*d*) Same as in panel *c* but at the Cu-L_3 ($2p \rightarrow 3d$) absorption edge. The scattering peak intensity (*orange dots and line*) is resonantly enhanced in the vicinity of the features of the absorption spectra (*green line*) corresponding to electronic transitions into the O and Cu sites in the CuO_2 planes. Adapted from Reference 74 with permission.

the evolution of the momentum-dependent interference fringes across the resonances was determined to be indicative of a rounding of the carrier density near the film-substrate interface. Most remarkably, the authors revealed the extent of resonant enhancement at these absorption edges in the cuprates, which amounts to a single doped hole in the CuO_2 planes scattering as strongly as 82 electronic charges, with a resulting magnification of the experimental signal equal to the square of the scattering amplitude, or $82^2 > 10^3$. This can be regarded as one of the key figures of merit for resonant X-ray methods and represents the foundational mechanism underlying the success of RXS in detecting weak ordering phenomena (such as charge order) in the cuprates.

Later, Abbamonte et al. (73) used RXS to discover and characterize the ordering of doped holes in the non-SC cuprate compound $Sr_{14}Cu_{24}O_{41}$. A peak in reciprocal space, representing the signature of a well-defined, periodic modulation of the electronic density along the reciprocal *L* axis and with wave vector $\mathbf{Q} = (0, 0, 0.2)$, could be measured only at the O-*K* pre-peak resonance at 528.6 eV (**Figure 3*b***), whereas no signal was detected once the photon energy was tuned off-resonance by only a few electronvolts (**Figure 3*a***). This work represents the very first RXS evidence of charge order in a copper-oxide compound, corresponding to the crystallization into a Wigner crystal phase, manifested as a modulation of the electronic charge triggered by electron-electron Coulomb interactions. This observation demonstrates the power of resonant scattering methods as opposed to conventional diffraction techniques, which, being nonresonant, are largely insensitive to subtle electronic ordering phenomena not involving the lattice degrees of freedom.

LBCO:
$La_{2-x}Ba_xCuO_{4+\delta}$

The first RXS study of charge order in one of the SC cuprate families came along in 2005, when Abbamonte et al. (74) investigated stripe order in $La_{2-x}Ba_xCuO_{4+\delta}$ (LBCO). Although the momentum structure of the stripe-ordered phases in this compound had been previously studied using neutron scattering (32), no direct information was yet available on the role and involvement of the electronic degrees of freedom, due to the fact that neutron scattering predominantly measures periodic distortions in the lattice. Abbamonte et al. found a peak in reciprocal space at (0.25, 0, L), consistent with previous observations (32) and with a weak dependence on the out-of-plane momentum L, thus confirming the prominent two-dimensional nature of the charge-ordered state. Once again, this study reaffirmed the fundamental role played by the resonant enhancement: **Figure 3*c,d*** shows the intensity of the charge-order peak (*red dots*) overlaid onto the absorption profiles (*green lines*) for the O-K and Cu-L_3 edges, respectively. The intensity for charge scattering is nonzero; i.e., it is detectable on top of the fluorescent background and above noise level, only near the oxygen prepeak (i.e., MCP) and the Cu excitonic resonance. This work had profound implications for the understanding of charge order in cuprates, because it clarified that stripe order is predominantly configured as a modulation of the electronic density followed by a distortion of the lattice, which represents a secondary effect, as demonstrated by the absence of any diffracted intensity away from the electronic resonances (in the soft X-ray range).

In the following sections, we provide a brief description of the theory of resonant scattering and of the experimental scheme. For a more comprehensive treatise on these topics, we refer the reader to References 68, 71, 72, 104, and 105, and references therein.

2.2. Theory of Resonant Scattering

RXS is a "photon in–photon out" technique, where photons get scattered from a material owing to their interaction with the electronic clouds. For radiation-matter scattering to occur, the interaction Hamiltonian has to contain operator combinations of the kind $a_\nu(\mathbf{q})a_\nu^\dagger(\mathbf{q}-\mathbf{Q})$, where $a_\nu^\dagger(\mathbf{q})$ [$a_\nu(\mathbf{q})$] is the operator creating (annihilating) a photon with wave vector $\mathbf{q}$, polarization state ν, and frequency $\omega = c\,|\mathbf{q}|$. The effective nonrelativistic interaction Hamiltonian can be derived from the full electron-matter minimal coupling Hamiltonian, and reads as follows:

$$\begin{aligned} H_{\rm tot} &= \sum\nolimits_j \left\{ \frac{1}{2m_e}\left[\mathbf{p}_j - \frac{e}{c}\mathbf{A}(\mathbf{r}_j,t)\right]^2 + V(\mathbf{r}_j,t)\right\} + \sum\nolimits_{j\neq k}\frac{e^2}{|\mathbf{r}_j-\mathbf{r}_k|^2} + H_{\rm EM} \\ &= \underbrace{H_{\rm el}+H_{\rm EM}}_{H_0} + \underbrace{\frac{e}{m_e c}\sum\nolimits_j \mathbf{A}(\mathbf{r}_j,t)\cdot\mathbf{p}_j}_{H_{\rm int}^{\rm lin}} + \underbrace{\frac{e^2}{2m_e c^2}\sum\nolimits_j \mathbf{A}^2(\mathbf{r}_j,t)}_{H_{\rm int}^{\rm quad}}, \end{aligned} \qquad 1.$$

where e and m are the fundamental electronic charge and mass, respectively; $\mathbf{p}_j$ and $\mathbf{r}_j$ represent the momentum and position coordinates of the j-th electron, respectively; and $V(\mathbf{r},t)$ and $e^2/|\mathbf{r}-\mathbf{r}'|^2$ are the lattice potential and the Coulomb interaction terms, respectively. $\mathbf{A}(\mathbf{r},t)$ represents the vector potential; $H_{\rm el} = \sum_j \frac{1}{2m_e}\mathbf{p}_j^2 + \sum_j V(\mathbf{r}_j,t) + \sum_{j\neq k}\frac{e^2}{|\mathbf{r}_j-\mathbf{r}_k|^2}$ is the Hamiltonian of the electronic system, whereas $H_{\rm EM} = \sum_{\mathbf{q},\nu}\hbar\omega[a_\nu^\dagger(\mathbf{q})a_\nu(\mathbf{q})+1/2]$ is the Hamiltonian of the electromagnetic (EM) field alone.

The interaction operators $H_{\rm int}^{\rm lin}$ and $H_{\rm int}^{\rm quad}$, which are, respectively, linear and quadratic in the vector potential, couple the EM field and the electronic degrees of freedom. At this point, we can use the states $|\Psi_M\rangle = |\psi_m\rangle_{\rm el} \times |\phi_{\bar{n}_{\mathbf{q},\nu}}\rangle_{\rm EM}$ as a basis set for the light-matter quantum system, where $|\psi_m\rangle_{\rm el}$ represents the electronic part of the wave function (with eigenvalues ϵ_m, and m labeling a generic set of quantum numbers) while $|\phi_{\bar{n}_{\mathbf{q},\nu}}\rangle_{\rm EM}$ indicates a photon state with photon occupation numbers $\bar{n}_{\mathbf{q},\nu} = \{n_{\mathbf{q}_1,\nu_1}, n_{\mathbf{q}_2,\nu_2},\ldots\}$, corresponding to having $n_{\mathbf{q}_1,\nu_1}$ photons with wave vector and

polarization ($\mathbf{q}_1$, ν_1), $n_{\mathbf{q}_2,\nu_2}$ photons with ($\mathbf{q}_2$, ν_2), and so on. In this notation, M labels the global set of quantum numbers; i.e. $M = \{m, \mathbf{q}, \nu\}$. Note that owing to the radiation-matter interaction, the states $|\Psi_M\rangle$ are not eigenstates of the system, but they can be used as a basis set in a perturbative scheme, in which case we define the unperturbed (i.e., with the interaction terms turned off) energy spectrum as $E_M = \epsilon_m + \sum_{\mathbf{q},\nu}(n_{\mathbf{q},\nu}\hbar\omega_{\mathbf{q}} + 1/2)$. Within this framework, a scattering process is defined as a transition from an initial photon state $|\phi_i\rangle_{\mathrm{EM}} = |...\rangle|n_{\mathbf{q}_{\mathrm{in}},\nu_{\mathrm{in}}}\rangle|n_{\mathbf{q}_{\mathrm{out}},\nu_{\mathrm{out}}}\rangle|...\rangle$ to a final photon state $|\phi_f\rangle_{\mathrm{EM}} = |...\rangle|n_{\mathbf{q}_{\mathrm{in}},\nu_{\mathrm{in}}} - 1\rangle|n_{\mathbf{q}_{\mathrm{out}},\nu_{\mathrm{out}}} + 1\rangle|...\rangle$, corresponding to the annihilation of an incoming photon with wave vector and polarization ($\mathbf{q}_{\mathrm{in}}$, ν_{in}) and the concomitant creation of an outgoing photon ($\mathbf{q}_{\mathrm{out}}$, ν_{out}).

Central in the theory of elastic scattering is the calculation of the probability of transition from a state $|\Psi_i\rangle = |\psi_{GS}\rangle_{\mathrm{el}} \times |\phi_i\rangle_{\mathrm{EM}}$ to a state $|\Psi_f\rangle = |\psi_{GS}\rangle_{\mathrm{el}} \times |\phi_f\rangle_{\mathrm{EM}}$, where the photon states $|\phi_i\rangle_{\mathrm{EM}}$ and $|\phi_f\rangle_{\mathrm{EM}}$ are as given in the previous paragraph and where we further assume that the electronic part of the initial and final state is in the ground state $|\psi_{GS}\rangle_{\mathrm{el}}$. The transition probability $w_{i\to f}$ between the initial and final quantum states can be calculated using the generalized Fermi's golden rule (106),

$$w_{i\to f} = 2\pi\left|\langle\Psi_i|T\,|\Psi_f\rangle\right|^2\delta\left(E_f - E_i\right), \qquad 2.$$

where the T-matrix is defined as follows:

$$T = H_{\mathrm{int}} + H_{\mathrm{int}}\frac{1}{E_i - H_0 + i\eta}H_{\mathrm{int}} + H_{\mathrm{int}}\frac{1}{E_i - H_0 + i\eta}H_{\mathrm{int}}\frac{1}{E_i - H_0 + i\eta}H_{\mathrm{int}} + \ldots. \qquad 3.$$

Here the first operator on the right-hand side represents the first-order perturbation term, the second operator represents the second-order perturbation term, and so on. In Equation 3, H_{int} is the interaction operator and H_0 is the unperturbed Hamiltonian—in our case $H_{\mathrm{int}} = H_{\mathrm{int}}^{\mathrm{lin}} + H_{\mathrm{int}}^{\mathrm{quad}}$ and $H_0 = H_{\mathrm{el}} + H_{\mathrm{EM}}$, respectively. In scattering, we require operator combinations of the kind $a^\dagger a$ inside the T-matrix, which originate from interaction terms that are quadratic in the vector potential $\mathbf{A}$, because the latter can be expressed in second-quantized notation as $\mathbf{A}(\mathbf{r}, t) \propto \sum_{\mathbf{q},\nu}\varepsilon_\nu \cdot [\exp(i\mathbf{q}\cdot\mathbf{r} - i\omega t)\, a_\nu^\dagger(\mathbf{q}) + h.c.]$ (ε_ν denoting the polarization vector of the polarization state ν). These combinations are generated by using the quadratic interaction operator $H_{\mathrm{int}}^{\mathrm{quad}}$ in the first-order term of Equation 3 and by the linear interaction operator $H_{\mathrm{int}}^{\mathrm{lin}}$ in the second-order term of Equation 3. The corresponding first- $[w_{i\to f}^{(1)}]$ and second- $[w_{i\to f}^{(2)}]$ order perturbative transition probabilities can then be obtained from Equation 2:

$$w_{i\to f}^{(1)} = 2\pi\left|\frac{e^2}{2m_e c^2}\langle\Psi_i|\sum\nolimits_j \mathbf{A}^2(\mathbf{r}_j, t)|\Psi_f\rangle\right|^2, \qquad 4.$$

$$w_{i\to f}^{(2)} = 2\pi\left|\left(\frac{e}{m_e c}\right)^2\sum\nolimits_M \frac{\langle\Psi_i|\sum_j \mathbf{A}(\mathbf{r}_j, t)\cdot\mathbf{p}_j|\Psi_M\rangle\langle\Psi_M|\sum_k \mathbf{A}(\mathbf{r}_k, t)\cdot\mathbf{p}_k|\Psi_f\rangle}{E_i - E_M + i\Gamma_M}\right|^2, \qquad 5.$$

where for convenience we have dropped the δ function (enforcing conservation of the total energy in the scattering process) originally present in Equation 2.

In Equation 5, Ψ_M represents a generic (excited) quantum state of the light-matter system, with corresponding energy E_M and lifetime $\hbar/\Gamma_M$. The squared vector potential can then be expanded as

$$\begin{aligned}\mathbf{A}^2(\mathbf{r}, t) &\propto \sum\nolimits_{\mathbf{q},\nu}\varepsilon_\nu\left[e^{i(\mathbf{q}\cdot\mathbf{r}-\omega t)}\, a_\nu^\dagger(\mathbf{q}) + h.c.\right] \times \sum\nolimits_{\mathbf{q}',\nu'}\varepsilon_{\nu'}\left[e^{i(\mathbf{q}'\cdot\mathbf{r}-\omega' t)}\, a_{\nu'}^\dagger(\mathbf{q}') + h.c.\right] \\ &\propto (\varepsilon_{\nu_{\mathrm{in}}}\cdot\varepsilon_{\nu_{\mathrm{out}}})\left[e^{i(\mathbf{q}_{\mathrm{out}}\cdot\mathbf{r}-\omega_{\mathrm{out}}t)}\cdot a_{\nu_{\mathrm{out}}}^\dagger(\mathbf{q}_{\mathrm{out}})\cdot e^{-i(\mathbf{q}_{\mathrm{in}}\cdot\mathbf{r}-\omega_{\mathrm{in}}t)}\cdot a_{\nu_{\mathrm{in}}}(\mathbf{q}_{\mathrm{in}})\right] \\ &\propto (\varepsilon_{\nu_{\mathrm{in}}}\cdot\varepsilon_{\nu_{\mathrm{out}}}) \times e^{\left[i(\mathbf{q}_{\mathrm{out}}-\mathbf{q}_{\mathrm{in}})\cdot\mathbf{r}\right]}\cdot a_{\nu_{\mathrm{out}}}^\dagger(\mathbf{q}_{\mathrm{out}})\, a_{\nu_{\mathrm{in}}}(\mathbf{q}_{\mathrm{in}}), \qquad 6.\end{aligned}$$

where $\varepsilon_{\nu_{\rm in}}$ and $\varepsilon_{\nu_{\rm out}}$ represent the polarization vector of the incoming and scattered photons, and in the last step of Equation 6, we assumed the scattering process to be elastic, i.e., $\omega_{\rm in} = \omega_{\rm out}$.

XRD: X-ray diffraction

At this point, by using the previous definitions for the initial and final states $|\Psi_i\rangle$ and $|\Psi_f\rangle$, respectively, together with the fact that $E_i = \epsilon_{\rm GS} + [n_{\mathbf{q}_{\rm in}}\hbar\omega_{\mathbf{q}_{\rm in}} + 1/2]$ and $E_M = \epsilon_{\rm m} + [(n_{\mathbf{q}_{\rm in}} - 1)\hbar\omega_{\mathbf{q}_{\rm in}} + 1/2]$, and considering that $a^{\dagger}_{\nu_{\rm out}}(\mathbf{q}_{\rm out})a_{\nu_{\rm in}}(\mathbf{q}_{\rm in})|\phi_i\rangle_{\rm EM} \propto |\phi_f\rangle_{\rm EM}$, we can rewrite Equations 4 and 5 as follows:

$$w^{(1)}_{i\to f} \propto \left|\langle\psi_{\rm GS}|\sum\nolimits_j e^{-i\mathbf{Q}\cdot\mathbf{r}_j}|\psi_{\rm GS}\rangle\right|^2 \propto |\langle\psi_{\rm GS}|\,\rho(\mathbf{Q})\,|\psi_{\rm GS}\rangle|^2, \qquad 7.$$

$$w^{(2)}_{i\to f} \propto \left|\sum_m\sum_{j,k}\frac{\langle\psi_{\rm GS}|\varepsilon_{\nu_{\rm in}}\cdot\mathbf{p}_j\cdot e^{i\mathbf{q}_{\rm in}\cdot\mathbf{r}_j}|\psi_m\rangle\langle\psi_m|\varepsilon_{\nu_{\rm out}}\cdot\mathbf{p}_k\cdot e^{-i\mathbf{q}_{\rm out}\cdot\mathbf{r}_k}|\psi_{\rm GS}\rangle}{\epsilon_{\rm GS}-\epsilon_m+\hbar\omega+i\Gamma_m}\right|^2, \qquad 8.$$

where $\mathbf{Q} = \mathbf{q}_{\rm in} - \mathbf{q}_{\rm out}$ is the momentum transferred by the photon field to the sample, and $\rho(\mathbf{Q})$ is the Fourier transform of the electron density operator $\rho(\mathbf{r}) = \sum_j \delta(\mathbf{r} - \mathbf{r}_j)$.

In the X-ray regime, the transition channel represented by Equation 8 involves the excitation of a high-energy many-body state with a core hole (ψ_m). In a more intuitive perspective, this is equivalent to the excitation of a core electron into an intermediate state through absorption of the first photon, followed by re-emission of a (scattered) photon once the core hole is filled back. By contrast, in the first-order perturbative term expressed by Equation 4, the scattering process does not involve the excitation of an intermediate state. As a consequence, the first-order mechanism (known as Thomson scattering), proportional to the squared amplitude of the total electronic density in the ground state, is nonresonant and controls the signal in conventional XRD. The second-order process is instead resonant and is, therefore, associated with RXS.

Equation 8 is a particular version of the Kramers-Heisenberg formula, which represents the general solution to the problem of a photon scattering from an electron. It can be further simplified under the assumption that the X-ray excitation process is local, which implies that (*a*) the local orbitals (at the lattice site *n*) can be used for the electronic basis set: $\psi_m(\mathbf{r}) \to \chi_l^{(n)}(\mathbf{r}) = \chi_l(\mathbf{r} - \mathbf{R}_n)$; (*b*) all matrix elements $\langle\chi_i^{(m)}|\mathbf{p}|\chi_l^{(n)}\rangle \propto \delta_{m,n}$ (i.e., they vanish for orbitals belonging to different lattice sites); and (*c*) due to the localization of the initial (core) electron around the position $\mathbf{R}_n$ of its parent atom, the phase due to the photon field can be approximated as $e^{i\mathbf{q}\cdot\mathbf{r}} \sim e^{i\mathbf{q}\cdot\mathbf{R}_n}$. At this stage, it is convenient to introduce a new quantity, the form factor f_{pq}, which is a photon energy– and site–dependent complex tensor defined as follows:

$$f^{(n)}_{pq}(\hbar\omega) = \frac{e^2}{m^2c^2}\sum_{i,l}\frac{\langle\chi_i^{(n)}|\mathrm{p}_q|\chi_l^{(n)}\rangle\cdot\langle\chi_l^{(n)}|\mathrm{p}_p|\chi_i^{(n)}\rangle}{\hbar\omega - (\epsilon_l^{(n)} - \epsilon_i^{(n)}) + i\Gamma_{il}}. \qquad 9.$$

Here $\chi_i^{(n)}$ and $\chi_l^{(n)}$ represent the initial and intermediate single-particle electronic states at site $\mathbf{R}_n$ (with energies $\epsilon_i^{(n)}$ and $\epsilon_l^{(n)}$, respectively) involved in the light-induced transition $i \to l$. Γ_{il} is the inverse lifetime ($\hbar/\tau_{il}$) of the intermediate state with an electron in $\chi_l^{(n)}$ and a hole in $\chi_i^{(n)}$. The resonant scattering cross section, through the form factor $f^{(n)}_{pq}(\hbar\omega)$, can be shown to bear a close connection to the X-ray absorption (i.e., XAS), which is a first-order process in the radiation-matter interaction Hamiltonian:

$$I^{\rm XAS}(\hbar\omega) \propto -\frac{1}{\omega^2}\times{\rm Im}\left[\sum\nolimits_n\sum\nolimits_p(\varepsilon_{\nu_{\rm in}})_p\cdot f^{(n)}_{pp}(\hbar\omega)\right], \qquad 10.$$

$$\begin{aligned} I^{\rm RXS}(\mathbf{Q},\hbar\omega) &\propto \left|\sum\nolimits_{pq}(\varepsilon_{\nu_{\rm in}})_p\cdot\left[\sum\nolimits_n f^{(n)}_{pq}(\hbar\omega)\,e^{i\mathbf{Q}\cdot\mathbf{R}_n}\right]\cdot(\varepsilon_{\nu_{\rm out}})_q\right|^2, \\ &= \left|\sum\nolimits_{pq}(\varepsilon_{\nu_{\rm in}})_p\cdot F_{pq}(\hbar\omega)\cdot(\varepsilon_{\nu_{\rm out}})_q\right|^2. \end{aligned} \qquad 11.$$

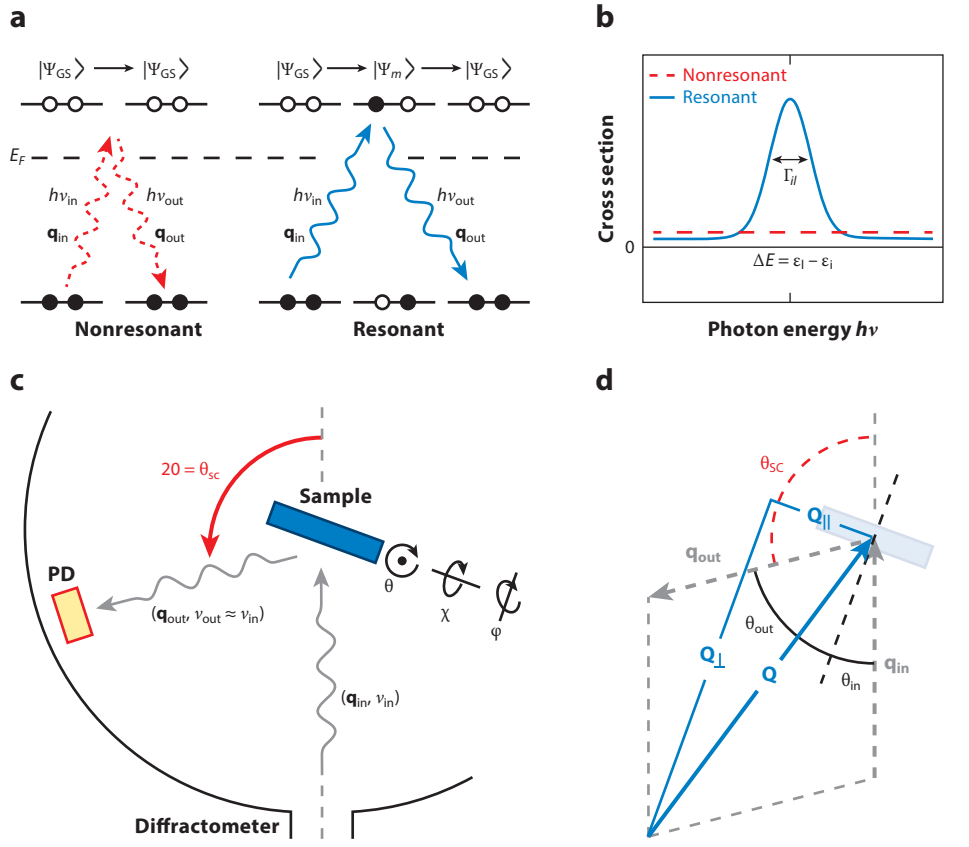

Figure 4

Resonant processes and scattering geometry in resonant X-ray scattering. (*a*) In nonresonant scattering the excitation process does not involve intermediate states, whereas resonant scattering occurs whenever the incident photon energy is tuned to promote an electronic transition from the ground state Ψ_{GS} to an intermediate state Ψ_m. The subsequent radiative recombination of the excited electron with the core hole results in the creation of an outgoing (scattered) photon. (*b*) The different photon energy dependence of resonant and nonresonant processes, showing the enhancement occurring in the resonant channel near an electronic transition with energy ΔE. (*c*) Schematics of a conventional diffractometer; kinematics for the scattering/diffraction process are outlined in panel *d*. Abbreviations: PD, photon detector; SC, scattering.

In Equation 11, F_{pq} represents the scattering tensor, which is not a local quantity (it does not depend on the lattice position $\mathbf{R}_n$) and is more directly related to the physical observable in RXS experiments (I^{RXS}). Moreover, from the above equations it follows that XAS only depends on the incoming light polarization $\varepsilon_{\nu_{in}}$, whereas the RXS signal depends on the outgoing light polarization $\varepsilon_{\nu_{out}}$, as well.

The difference between resonant and nonresonant scattering is schematized in **Figure 4*a***. The mechanism corresponding to XRD involves a single step, by virtue of its first-order nature; conversely RXS, being a second-order transition, proceeds in two stages involving an intermediate state. This is clearly reflected in the very different photon energy ($h\nu$) dependence of the two channels (see **Figure 4*b***): Whereas XRD is nearly energy-independent (*red dashed curve*), the cross section for RXS is strongly peaked around the energy of the electronic transition (*blue curve*), where the experimental signal undergoes a strong enhancement (while decaying to zero away from

the resonance). Such enhancement is typically realized at an absorption edge, i.e., when electronic transitions from a deeply bound core state into the valence band (and beyond into the continuum) take place. As a consequence, RXS gains a strong sensitivity [as large as 82-fold in the cuprates (74, 100)] to partial modulations of the charge density involving a single electronic band, whereas the XRD signal reflects the total electronic density (see Equation 7) and therefore suffers from a weak sensitivity to spatial variations of the latter, unless they are accompanied by a distortion of the lattice, which would involve all the electrons (core and valence).

2.3. The Experimental Scheme

In an actual scattering or diffraction experiment, a monochromatic X-ray beam with wave vector $\mathbf{q}_{\text{in}}$, photon energy $\hbar\omega_{\text{in}} = c \cdot q_{\text{in}}$, and polarization $\varepsilon_{\nu_{\text{in}}}$ impinges on a sample and a scattered photon will be detected along the direction of the wave vector $\mathbf{q}_{\text{out}}$ using an energy-integrating photon detector or an energy-resolving spectrometer (see **Figure 4*c***). At the end of the process, a net momentum and energy have been transferred to the sample, which can be derived from the corresponding conservation laws:

$$h\nu_{\text{in}} = h\nu_{\text{out}} + \Delta E, \qquad 12.$$

$$\mathbf{q}_{\text{in}} = \mathbf{q}_{\text{out}} + \mathbf{Q}. \qquad 13.$$

In the case of elastic scattering $h\nu_{\text{in}} = h\nu_{\text{out}}$ and there is no energy transfer with the sample ($\Delta E = 0$), whereas the case $\Delta E \neq 0$ defines inelastic scattering events. Strictly speaking, elastic scattering probes the static component of the charge and magnetization density occurring in the system under study, whereas inelastic scattering is sensitive to dynamical processes and low-energy excitations. However, due to the spectrometer-characteristic finite energy resolution δE (which in the soft X-ray regime ranges between 30 meV and 1 eV, whereas hard X-ray spectrometers reach down to 1 meV), purely elastic scattering cannot be experimentally accessed, and it is more appropriate to use the term quasi-elastic scattering, which probes a regime that is static up to a timescale $\tau \sim \hbar/\delta E$. From a more practical standpoint, the energy-integrated measurement in most cases yields a reliable representation of the momentum structure of the ordered state, owing to fact that the inelastic part of the spectra usually evolves very smoothly and can be discarded as background in RXS, especially if it exhibits a different temperature dependence with respect to the zero energy-loss feature (see also discussion of **Figure 5**).

Hereafter, we focus on the momentum structure of RXS measurements and, unless otherwise specified, assume the use of the energy-integrated mode. From Equation 13, and using $h\nu_{\text{in}} = h\nu_{\text{out}}$, the magnitude of the exchanged momentum can be expressed as $Q = 2\, q_{\text{in}} \times \sin(\theta_{\text{sc}}/2)$ (θ_{sc} is the scattering angle; see **Figure 4*c***). Projecting $\mathbf{Q}$ into the plane defining the sample surface then yields the in-plane ($\mathbf{Q}_{\parallel}$) and out-of-plane ($\mathbf{Q}_{\perp}$) components of the transferred momentum, which will be often referenced in the rest of this work (see **Figure 4*d***). The realization of this geometry is illustrated in **Figure 4*c*** and described in greater detail in Reference 95. In general the photon detector moves on a single circle; that is, a single angular goniometer (the corresponding variable is often denominated 2θ and corresponds to the scattering angle θ_{sc}). The sample stage usually involves translational motion (xyz) and various rotations, whose number defines the type of diffractometer. Two-circle diffractometers represent the most common choice for soft X-ray experiments, featuring a single angular motion (with angular variable denominated θ) for the sample (first circle), whose axis is perpendicular to the scattering plane (the one spanned by the vectors $\mathbf{q}_{\text{in}}$ and $\mathbf{q}_{\text{out}}$), in addition to the detector rotation (2θ), which represents the second circle. The first generation of soft X-ray diffractometers also includes two additional rotational degrees

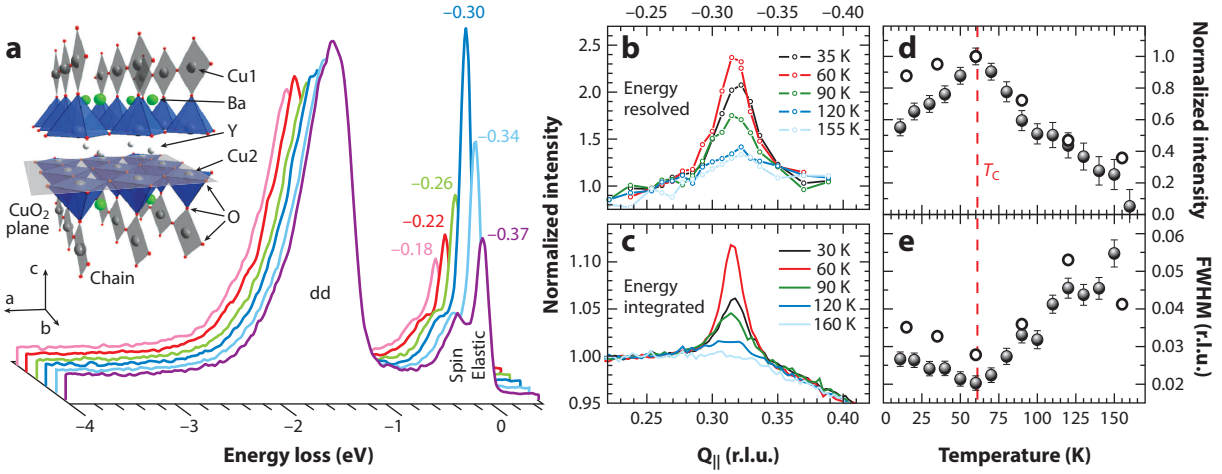

Figure 5

Resonant X-ray scattering discovery of charge-density waves in (Nd,Y)$Ba_2Cu_3O_{6+x}$. (*a*) Resonant inelastic X-ray scattering (RIXS) measurements of underdoped $Nd_{1.2}Ba_{1.8}Cu_3O_7$ ($T_c = 65$ K) as a function of energy loss and momentum [along (*H*00)], showing the emergence of a quasi-elastic peak around $H \sim -0.31$ r.l.u.; inset: three-dimensional view of the lattice structure of $YBa_2Cu_3O_{6+x}$. Note: "dd" indicates intraband transitions. (*b*,*c*) Momentum dependence of the (*b*) quasi-elastic and (*c*) energy-integrated RXS intensity for a series of temperatures across the superconducting transition T_c. (*d*,*e*) Temperature evolution of (*d*) the charge-order peak intensity and (*e*) full-width-at-half-maximum (FWHM), showing a cusp at T_c, thereby providing evidence of competition between charge order and superconductivity. Adapted from Reference 130 with permission.

of freedom (denominated χ and ϕ; see again **Figure 4*c***), allowing a fine alignment of the sample axes with respect to the scattering plane (however, χ and ϕ typically cover a limited angular range of −5° to 5°). New designs are being developed using different geometries to extend the angular range and control for the sample orientation. Diffractometers with more circles (up to 6, including 3 for the sample and 3 for the detector) covering an ample angular range are routinely used at higher photon energies (hard X-rays, $\hbar\omega > 7$ keV), where the added complication of the all-vacuum environment required for soft X-rays is lifted. Consequently, hard X-ray diffractometers can typically access a wider portion of reciprocal space.

Typically, the experimental signal is comprised of both resonant and nonresonant contributions, and in the two possible regimes $w_{fi}^{(XRD)} \gg w_{fi}^{(RXS)}$ or $w_{fi}^{(RXS)} \gg w_{fi}^{(XRD)}$ one ends up probing different phenomena (see again **Figure 4*b***). In the first case, where nonresonant processes are dominant, all electrons contribute equally to the measured signal, which is therefore simply proportional to the atomic number *Z*. The diffraction signal will be dominated by the core electrons, which usually outnumber the valence ones ($n_{core} \gg n_{valence}$), with the exception of lighter elements that, as a result, are not probed very effectively in XRD. In addition, because core states are very tightly bound to their parent nucleus, in a conventional diffraction experiment one mainly probes the ionic lattice in reciprocal space, which is why XRD is used primarily for structural studies. In the second case, the scattering process has a strong enhancement that corresponds with a very specific electronic transition. As a result the signal bears the signature of the electronic distribution (in reciprocal space) of the final state of such a transition. This characteristic of resonant scattering allows it to be not only element-specific (whenever the absorption edges of different chemical species are spaced sufficiently apart in photon energy) but also orbital-selective. This unique capability of RXS has been established and employed in many different systems. Charge ordering in cuprates (74) and cobaltates (107) and orbital-ordering in the manganites (92, 108, 109) are among the most spectacular case studies.

3. CHARGE ORDER IN CUPRATES—A NEVER-ENDING JOURNEY

3.1. A Resurging Phenomenology: Charge-Density Waves in YBCO

LESCO: $La_{2-x-y}Eu_ySr_xCu_2O_{4+\delta}$

Fifteen years after the original discovery of stripe order by Tranquada et al., charge order had been observed in the doping region around 12% hole doping directly in the three families of La-, Bi- and Ca-based cuprates: LNSCO (30, 31, 33, 38, 110), LBCO (32, 74, 110, 111), and LESCO (112, 113) using neutron and X-ray scattering (in the studies of References 112 and 113, RXS was used, in particular); and Bi2212 (35, 39, 41–43, 50, 51, 114–119), Na-CCOC (42, 43), and Bi2201 (46) using STM. However, no clear evidence of charge order had been found in the YBCO compounds, where the possibility of introducing doped carriers via the fractional filling of the Cu-O chain layer helps reduce the electronic inhomogeneity in the CuO_2 planes (120).

The first indication of electronic order in YBCO came in 2007 thanks to a series of pioneering measurements at high magnetic fields (up to 62 T) and low temperatures (down to 1.5 K) revealing the presence of quantum oscillations in the Hall resistance R_{xy} in the normal state of underdoped $YBa_2Cu_3O_{6.51}$ ($p = 0.10$, $T_c = 57$ K) samples (121, 122). The frequency of these oscillations versus the inverse magnetic field provided evidence for the emergence of small Fermi pockets at high fields (121), which are arguably of an electron-like nature in light of the negative sign for the Hall coefficient R_H (122). These findings indicated a change in the Fermi surface topology from the large hole-like Fermi "barrels" in the overdoped regime (123, 124) to smaller pockets in the underdoped regime, thereby suggesting "a reconstruction of the Fermi surface caused by the onset of a density-wave phase, as is thought to occur in the electron-doped copper oxides near the onset of AF order" (122, p. 1). The striking similarity between the Hall and Seebeck coefficients of YBCO and those of LESCO (125–127) made a strong case for a type of order in YBCO akin to the stripe order in LESCO. The first direct evidence that the Fermi surface reconstruction is due to charge order was provided by high-field nuclear magnetic resonance (NMR) measurements on $YBa_2Cu_3O_{6.54}$ ($p = 0.104$, $T_c = 57$ K), where a splitting in the ^{63}Cu(2) lines was observed at 28.5 T and below 50 K, signaling a change in the quadrupole frequency that was ascribed to a periodic variation in the charge density at planar Cu sites or at the O sites bridging them (128). The simplest scenario seemingly compatible with the NMR results was a unidirectional density modulation with $4a$ (four unit cells) periodicity. Furthermore, the observation of the charge-order-induced NMR splitting for strong fields perpendicular but not parallel to the conducting CuO_2 planes provided evidence of a competition between superconductivity and charge order.

The quantum oscillations and NMR results seemed to point to the necessity of completely suppressing superconductivity to observe the emergence of a seemingly competing charge-ordered state. Following early RXS explorations by Hawthorn et al. (129), the first direct observation of a charge-density wave in reciprocal space, and at zero magnetic field, was obtained in 2012 by Ghiringhelli et al. (130) using energy-resolved and energy-integrated RXS on a series of YBCO doping levels around 12%. The central experimental data uncovering the momentum location, and therefore the periodicity, of charge order in YBCO are shown in **Figure 5*a*** and consist of a series of scans of the X-ray energy loss (*horizontal axis*) for different values of the planar projection (H) of the momentum $\mathbf{Q} = (H, K, L)$ along the ($H0L$) direction in reciprocal space. The energy structure of the RIXS spectra bears three main contributions: (*a*) a quasi-elastic line at zero energy loss, (*b*) a low-energy peak/shoulder representing spin excitations, and (*c*) intraband (dd) particle-hole excitations. Although the spectral weight of the spin and dd excitations is nearly momentum-independent, a clear enhancement of the quasi-elastic line can be seen around a planar momentum $H \sim -0.31$ r.l.u., which reveals the presence of a periodic modulation of the electronic density; this reflects the momentum structure of a zero-field ordered state possibly connected to the one previously identified with NMR [recent high-field diffraction measurements, which are

discussed later, helped clarify the nature of this connection (131)]. The RXS data further revealed charge modulations to be present along both planar crystallographic axes, albeit with different amplitudes (as discussed more extensively in Reference 132. The same momentum-space peak can be equally well identified following the quasi-elastic component in energy-resolved spectra (**Figure 5*b***) and the energy-integrated RXS (**Figure 5*c***), which confirms (*a*) the importance of the resonant enhancement at the Cu-L_3 edge and that (*b*) only the quasi-elastic scattering contributes to a pronounced momentum-resolved structure, as previously discussed.

The detailed temperature dependence of energy-resolved and energy-integrated RXS momentum scans in **Figure 5*b,c*** points to an onset temperature of $T \sim 150$ K and, most importantly, to a partial suppression of the charge-order peak below the SC transition temperature T_c. This finding provides direct evidence of a competition between superconductivity and charge order and is further substantiated by the temperature evolution of the charge-order peak intensity and full-width-at-half-maximum (FWHM, inversely proportional to the correlation lengths) reported in **Figure 5*d*** and **5*e*** for the case of energy-resolved and energy-integrated RXS, respectively. The intensity and FWHM data indicate a clear weakening of the charge-ordered state in both its amplitude and spatial correlations at the emergence of the SC state. Around the same time, the wave vector of the charge-density wave in YBCO and its competition with the SC state were measured by nonresonant hard XRD experiments, which revealed an enhancement of the charge-order amplitude below T_c when superconductivity was actively weakened by applying magnetic fields up to 17 T (133). Field-induced enhancement of charge order was similarly reported in LBCO using hard XRD (134).

The discovery and identification of the charge-order state in YBCO represented a breakthrough in the field of copper-oxide superconductors, as it suggested that the charge-ordered state could be a defining instability of the CuO_2 planes, and strongly contributed to revitalizing this research direction. Stimulated by the possibility to provide a unifying view of charge order in the cuprates, intense efforts at the experimental and theoretical levels were put forth in order to identify a common thread across the different manifestations of charge order that emerged over the years.

A series of studies analyzed the photon energy dependence of the charge-order signal from LESCO (112), LNSCO (135), and YBCO (136), which is inherited from the photon energy dependence of the complex form factor $f(\hbar\omega)$ (see Equations 9 and 11). The imaginary part of the latter is directly related to the X-ray absorption signal, and the real part can be extracted by a Kramers-Kronig transformation. For a transition into a single Cu-$3d_{x^2-y^2}$ hole (which is the case at the Cu-L_3 edge in the cuprates) there is no multiplet structure, and the (site-dependent) form factor can be approximated by a simple Lorentzian lineshape as $f^{(n)} \sim A_n(\hbar\omega - \varepsilon_n + i\Gamma)^{-1}$, so that the RXS intensity can be expressed as

$$I^{\mathrm{RXS}}(\mathbf{Q}, \hbar\omega) \propto \left|\sum\nolimits_n f^{(n)}(\hbar\omega)\, e^{i\mathbf{Q}\cdot\mathbf{R}_n}\right|^2 = \left|\sum\nolimits_n \frac{A_n}{(\hbar\omega - \varepsilon_n + i\Gamma)} e^{i\mathbf{Q}\cdot\mathbf{R}_n}\right|^2, \qquad 14.$$

where the polarization dependence has been neglected for simplicity. Equation 14 shows that there are three variables controlling the RXS signal that can vary spatially: (*a*) the transition amplitude A_n, (*b*) the lattice position $\mathbf{R}_n$, and (*c*) the transition energy ε_n. Correspondingly, Achkar et al. evaluated the impact on the RXS signal of assuming a periodic modulation for (see **Figure 6*a***) (*a*) the valence modulation, (*b*) the lattice displacements, and (*c*) the transition energy shifts (this term was introduced in References 136 and 135). The comparison between the experimental RXS peak amplitude and the model calculations versus photon energy is shown in **Figure 6*b*** for LNSCO and in **Figure 6*c*** for YBCO. In both cases, the RXS signal is predominantly controlled by the spatial variation of the X-ray transition energy shifts, whereas in the earlier work on LESCO the RXS lineshape was explained by the nonlinear increase of the charge-carrier peak as a function

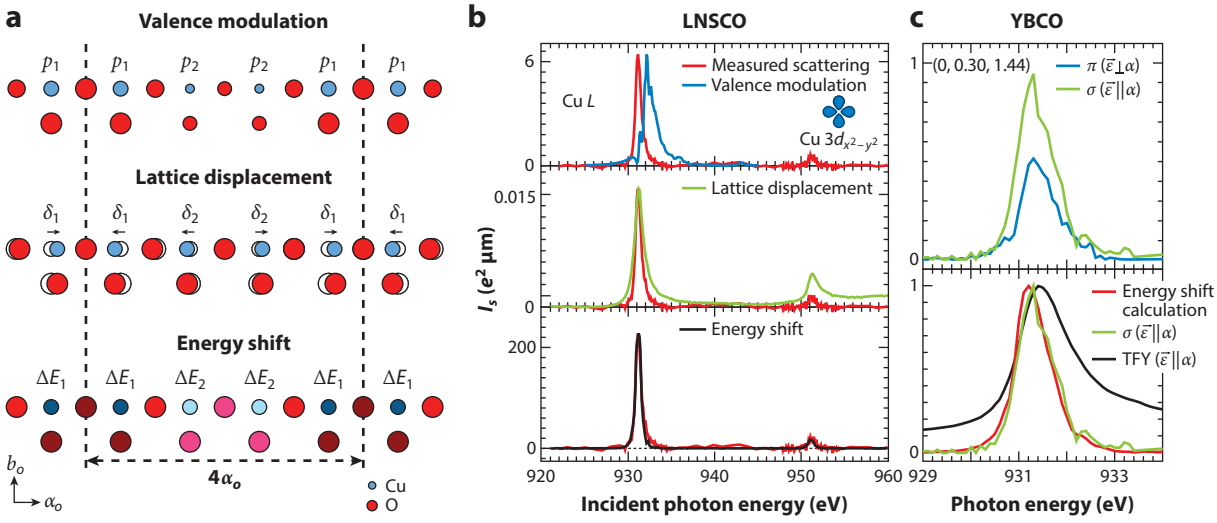

Figure 6

Photon energy–dependent resonant X-ray scattering (RXS) from charge order in cuprates. (*a*) Schematic representation of the possible microscopic contributions to the RXS signal: (*top*) valence modulation, (*middle*) lattice displacement, and (*bottom*) transition energy shift. (*b*) Comparison of the photon energy–dependent RXS intensity from the stripe-order peak in $La_{2-x}Ba_xCuO_{4+\delta}$ to calculations from the models introduced in panel *a*, showing that the resonant scattering signal is predominantly controlled by spatial variations in the X-ray transition energies. Adapted from Reference 135 with permission. (*c*) Photon energy–dependent RXS signal from charge order in $YBa_2Cu_3O_{6+x}$ (YBCO) for (*top*) horizontal (π) and vertical (σ) incoming polarization and (*bottom*) comparison between experiment and the prediction of the energy-shift model for polarization along the **a** axis. Abbreviation: TFY, total fluorescence yield. Adapted from Reference 136 with permission.

of doping p owing to a reduction of correlation effects (U) at higher doping concentrations. More recently, an alternative theoretical framework has been devised that explains the photon energy–dependent RXS signal by accounting for the delocalized character of intermediate states (137).

A closely following series of studies provided a complete mapping of the detailed characteristics of this phenomenology—the relative amplitude of the order parameter between YBCO and LBCO (138), the connection between charge order and magnetic instabilities (139–141), the origin of finite correlations and the role of disorder in the chain layer (142), and the feedback on lattice dynamics (143–145), and the pattern of atomic displacements accompanying electronic modulations in the charge-ordered state (146). This tremendous amount of progress made it possible to shed new light on the role of charge order within the phase diagram and its connection to coexisting and neighboring electronic orders and phases. The complete doping dependence of the salient properties of charge order in YBCO, and its comparison to La-based cuprates, were reported by Blanco-Canosa et al. (132) and Hucker et al. (141) .

One of the open questions is the connection between the charge order seen in high magnetic fields via NMR (128, 147) and the charge modulations seen in zero field via XRD. A field-induced thermodynamic phase transition was detected in the sound velocity of underdoped YBCO (148), suggesting that the high-field and low-field states are distinct, and in particular that the high-field charge order is two-dimensional in nature. NMR measurements, owing to their ability to probe both the high-field and the zero-field regimes, also established that charge order in these two regimes manifests itself as distinct phases, which furthermore coexist at low temperatures and high fields (149). A recent XRD study in pulsed magnetic fields up to 28 T revealed that there is

indeed a field-induced crossover from a short-ranged order to long-ranged charge modulations with different period along the **c** axis (131).

NdBCO: $NdBa_2Cu_3O_{6+x}$

3.2. Unifying Real and Reciprocal Space: Bi2201 and Bi2212

The discovery of charge-density waves in YBCO reinforced the idea that charge order might be a genuinely universal instability of the CuO_2 planes, and the combination of real-space (STM) and reciprocal space (neutron scattering, XRD, RXS) techniques had provided support for one and the same underlying general phenomenology in underdoped cuprates around 12% hole doping. Despite such mounting evidence and the several unifying traits linking the various cuprate families, the real-space phenomenology of charge order in Bi-based compounds appeared very granular, at variance with the well-defined structures in reciprocal space as observed by scattering probes in La- and Y-based cuprates. The very different probing depth—a few ångströms for STM versus hundreds of nanometers (and more) for scattering techniques—and a possible dichotomy between surface and bulk [as observed for charge-density waves along the Cu-O bond direction in LSCO (150) and along the zone diagonal in Bi2201 (151)] also contributed to a perceived disconnect between the domains (real space/surface versus momentum space/bulk) and materials (Bi- versus La- and Y-based cuprates) investigated by these two classes of experimental methods.

Two recent works (49, 152) addressed this aspect by investigating charge order on the same materials using STM and RXS. Due to the complications in exposing atomically flat surfaces in any cuprate material other than Bi-based compounds, these two studies were performed on La-doped Bi2201 (in the doping range $0.11 < p < 0.14$) (152) and Bi2212 (in the doping range $0.07 < p < 0.13$) (49). In Bi2201, charge order was found with a wave vector between 0.243 and 0.265 r.l.u. for decreasing doping, whereas in Bi2212 the ordering wave vector spans across a more extended range, from 0.25 to 0.31 r.l.u.; this is a finding that was later corroborated by the detection of charge order in optimally doped Bi2212 ($p \sim 0.16$, $T_c = 98$ K) (153). Most importantly, both studies demonstrated that the LDOS modulations imaged by STM and the reflections measured by RXS in reciprocal space originate from the very same microscopic entity. This is shown in **Figure 7*a*,*b*** by the comparison between the RXS momentum scans (panel *a*) in underdoped Bi2201 ($T_c = 15$ K, $p \sim 0.11$), revealing a charge-order peak emerging at low temperature at $\mathbf{Q} \sim (0.265, 0, L)$, and the Fourier-transformed differential conductance data (panel *b*) taken on the very same samples, which exhibit a peak at the same momentum value. A similar correspondence was found in Bi2212. The temperature dependence of the RXS charge-order peak for three different Bi2201 doping levels is reported in **Figure 7*c***, showing a very gradual onset of the density modulations that occurs on a temperature scale that is proximate to the pseudogap temperature T^* as determined from Knight shift measurements (154). In Bi2212, RXS data also reveal a rather slow temperature evolution of the peak intensity, which is accompanied by a drop below T_c. Although this drop is smaller than its analog in YBCO (130, 133, 136), the competition with superconductivity is clearly demonstrated by temperature-dependent STM measurements that also reveal that the charge order is more pronounced for the unoccupied states (49). Furthermore, in Bi2201 comparison between the RXS results and the Fermi surface measured using angle-resolved photoemission spectroscopy revealed a quantitative link between the observed charge-order wave vector and the momentum vector connecting the tips of the Fermi arcs, which in this case coincide with the so-called hot spots (see **Figure 7*d***). This correspondence suggests a possible link between the density modulations and the low-energy electronic structure, an element that is consistent with the doping evolution of the wave vector and that had been hinted at by previous studies (46, 155). Recent theoretical works have discussed the possible special role played by the hot spots in the context of a magnetically driven charge-order instability (13, 156–159), as well as the possibility

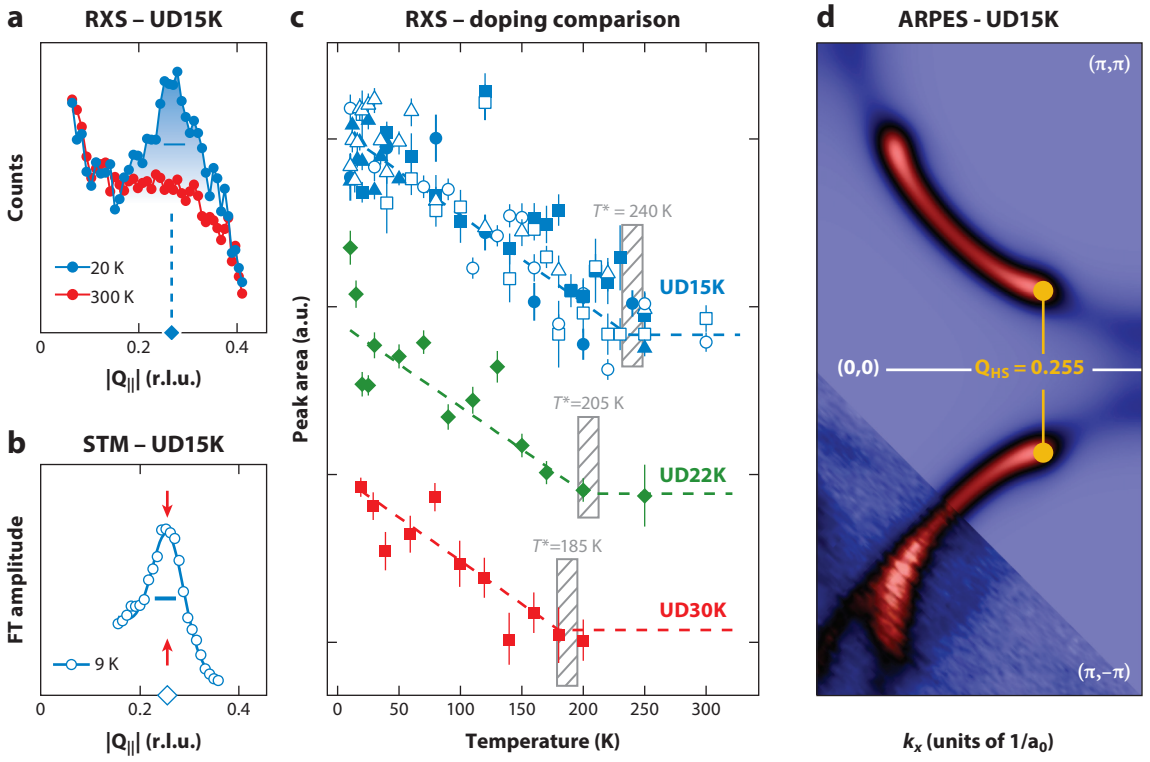

Figure 7

Resonant X-ray scattering (RXS) and scanning tunneling microscopy (STM) joint evidence of charge order in $Bi_2Sr_2CuO_{6+\delta}$. (*a*) RXS scans along (*H*00) for an underdoped ($T_c \sim 15$ K) Bi2201 at low (*blue*) and high (*red*) temperature, showing the emergence of a broad charge-order peak around $H \sim 0.25$ r.l.u. (*b*) (*H*00) line cut of the Fourier-transformed differential tunneling conductance on freshly cleaved surfaces of the same Bi2201 samples, indicating the equivalence of the charge modulations detected using STM. (*c*) Temperature dependence of the charge-order peak intensity (from RXS) for three doping levels ($T_c \sim 15$ K, 22 K, and 30 K) in the under-to-optimal doping range, and correlation of the charge-order onset with the pseudogap temperature T^* (*gray boxes*). (*d*) Experimental (*bottom*) and calculated (*top*) Fermi surface for UD15K Bi2201, highlighting the Fermi arcs characterizing the pseudogap regime, and the wave vector (*yellow connector*) linking the arc-tips, or hot spots, in agreement with the RXS experimental results. Adapted from Reference 152 with permission. Abbreviation: ARPES, angle-resolved photoemission spectroscopy.

that charge order might arise from a $2Q$ instability of the antinodal points within a pair-density-wave framework (160). Additionally, we note that the RXS detection of charge order around $Q \sim 0.25$ r.l.u. in Bi2201 confirms previously unpublished findings of a phonon anomaly at the same momentum location using inelastic X-ray scattering (161), which might be suggestive of a related anomaly in the electronic susceptibility or otherwise of a strongly momentum-dependent electron-phonon coupling mechanism at work.

3.3. Toward a Universal Phenomenology: Charge Order in Hg1201 and NCCO

In the wake of the results on Y- and Bi-based cuprates, evidence had been mounting that charge order could be a universal phenomenon in the cuprates. In 2012, Wu et al. detected charge order in the prototypical superconductor LSCO around a doping of 12% (150); this discovery revealed that the low-temperature tetragonal structure in La-based cuprates is not essential for the appearance of stripe order (but perhaps relevant for stabilizing it). In this study, the comparison between

resonant and nonresonant scattering data was interpreted in terms of a surface enhancement of the stripe order in LSCO. More recently, stripe order was found in the bulk of LSCO using XRD (162, 163) and RXS (164).

Hg1201: $HgBa_2CuO_{4+\delta}$

Having exhausted all other families, Hg-based cuprates remained the last hole-doped family to be investigated. In particular, $HgBa_2CuO_{4+\delta}$ (Hg1201) represents the only series of compounds with a pristine, tetragonal unit cell, therefore possessing the highest structural symmetry among all cuprates. The first indirect evidence of broken translational symmetry in Hg1201 came from the discovery of Fermi-surface reconstruction via high-field measurements of the Hall and Seebeck coefficients in underdoped Hg1201 (165), followed by the detection of quantum oscillations (166). In 2014, Tabis et al. reported the very first evidence of charge order below 200 K in underdoped ($p \sim 0.09$, $T_c = 72$ K) Hg1201 from RXS and RIXS measurements (167). The charge-order peak was found at $Q \sim 0.28$ r.l.u.—which is comparable with the values found in Bi2212 and intermediate between YBCO and La-based compounds—and required using resonant excitation, indicating that charge order is a rather subtle phenomenon in the Hg1201. This instance, combined with the fact that Hg1201 exhibits record-high T_c among single-layered cuprates, suggests a possible anticorrelation between charge order and superconductivity. Furthermore, the study revealed a direct connection between the onset of charge correlations and T^{**}, "the temperature at which the Seebeck coefficient reaches its maximum value, and below which conventional Fermi-liquid planar charge transport is observed" (167, p. 3). It also suggested a possible common origin of the main instabilities in the CuO_2 planes, namely "the possibility that the sequence of ordering tendencies ($q = 0$ order precedes charge order, which in turn precedes SC order) and the phase diagram as a whole are driven by short-range antiferromagnetic correlations" (167, p. 5). Lastly, Tabis et al. successfully established the link between the charge order–induced reconstruction of the Fermi surface and the size of the electron pockets observed by quantum oscillations in YBCO (121, 122) and Hg1201 (166), and they were able to correctly predict the QO frequencies over an extended doping range. More recent X-ray diffraction measurements additionally found charge order in Hg1201 at 12% hole doping and explored the spatial topography of the ordered state (168).

Figure 8 provides a graphical compendium of all charge-order observations in the hole-doped cuprates for what concerns the doping dependence of the onset temperature (**Figure 8*a***) and of the wave vector (**Figure 8*b***) as observed using both spatial-resolved (*open symbols*) and momentum-resolved (*filled symbols*) probes. The shaded phase diagram in **Figure 8*a*** is representative of YBCO and includes the AF phase near zero doping and the SC dome at higher hole doping levels. All colored lines are guides-to-the-eye, except for the $Q = 2p$ line, which interpolates the doping dependence of the ordering wave vector in LSCO below 12% doping according to the picture of perfect stripes with 1/2 hole per unit cell along the charged rivers. Note that the points from References 38 and (169) are from neutron scattering measurements of the AF peaks in LSCO, from which the charge-order wave vector Q_{CO} was derived using the phenomenological relation $Q_{CO} = 2\,Q_{AF}$. It is clear from the phase diagram of **Figure 8*a*** how in all cases charge order emerges at the highest temperature scales around 12% hole doping and spans a doping range tentatively bound by two endpoints[4] (52, 54, 171, 172), thereby hinting at a possible intimate connection between this phenomenology and quantum criticality (173, 174). Interestingly, the onset temperatures appear to scale inversely with the charge-order amplitudes and, correspondingly, correlation lengths (which are at maximum for La-based cuprates, intermediate for YBCO, and weak in the case of Bi-based compounds). At the same time, the extent of the suppression of T_c near 12 % doping is larger for the

[4]Note, however, that recently charge order has been observed in YBCO in the very underdoped regime, at $p \sim 0.058$ ($T_c \sim 12.6$ K), along the K reciprocal axis only, with wave vector $Q_{CO} \sim 0.337$ r.l.u. and onset temperature $T_{CO} \sim 65$ K (170).

families exhibiting stronger charge order, which is consistent with the experimentally observed competition between these two instabilities. Finally, we note that two main phenomenological differences exist between the stripy La-based cuprates and all other families: (*a*) In La-based compounds charge order and incommensurate AF spin order are simultaneously present, whereas they are mutually exclusive in the other compounds; (*b*) the doping evolution of the charge-order wave vector exhibits the opposite sign for La-cuprates with respect to the other families, which are putatively compatible with a nesting scenario (see also guides-to-the-eye in **Figure 8*b***). There are therefore strong indications for a common charge instability in all families of doped cuprates, but at the same time there are also stark differences between the manifestations of charge order in the conventional stripy compounds and in all other families.

NCCO: $Nd_{2-x}Ce_xCuO_{4+\delta}$

With charge order consistently detected across all flavors of hole-doped cuprates around 12% doping, the next frontier to be crossed was represented by the exploration of the electron-doped side of the phase diagram. Early insights came from inelastic X-ray scattering work (175) reporting anomalies in the dispersion of optical phonons in $Nd_{2-x}Ce_xCuO_{4+\delta}$ (NCCO), followed by quantum oscillation studies providing evidence for a reconstructed small-pocket Fermi surface in the same compound (176) and, more recently, by evidence from time-resolved studies of a broken-symmetry phase (177). Recently, the first hints of charge order were reported by Lee et al. (178) and Ishii et al. (179), who used RIXS to map out the momentum-dependent structure of low-energy bosonic excitations in NCCO for electron-doping values spanning the phase diagram from the AF to the SC phase. In both studies, RIXS measurements revealed the presence of spin waves associated with the AF order at low doping, which evolved into paramagnon excitations in the SC state ($x \sim 0.15$). Around this doping, an additional branch of a rapidly dispersing, gapped excitation was found, which was interpreted as a particle-hole excitation in Reference 179 and as a charge amplitude mode in Reference 178, therefore suggesting the possible signature of a symmetry-broken quantum state over an extended temperature range beyond the SC phase.

Direct evidence for charge order in NCCO was obtained by Da Silva Neto et al. (180) by means of RXS measurements in reciprocal space, which revealed a broad reflection at a wave vector $Q \sim 0.25$ r.l.u., i.e., very proximate to the findings in hole-doped cuprates, once again pointing to a unified phenomenology and a possible universal instability of the CuO_2 planes. The RXS scans for a SC NCCO sample ($x = 0.14$) are shown in **Figure 9*a*,*b*** as a function of photon energy and temperature, respectively. The charge-order peaks are rather broad, with correlation length $\xi \sim$ 25–35 Å, smooth evolution as a function of temperature, and a finite peak amplitude persisting up to rather high temperatures (350–400 K), as reported in **Figure 9*c***. Such a high onset temperature rules out a direct connection of charge order with the pseudogap phenomenology in electron-doped cuprates; instead, the charge-order signal appears to partly correlate with the temperature evolution of the AF fluctuations in the same material (181), uncovering a possible connection

Figure 8

Charge-order onset temperature and wave vector for all cuprate families. (*a*) Onset temperatures of charge order versus hole doping, for all cuprate families. The shading in the background outlines the boundaries of the antiferromagnetic (AF), superconducting (SC), and pseudogap (PG) regimes in $YBa_2Cu_3O_{6+x}$ (YBCO). (*b*) Doping dependence of the charge-order wave vector [the $La_{2-x-y}Nd_ySr_xCu_2O_{4+\delta}$ (LNSCO) and $La_{2-x}Sr_xCuO_4$ (LSCO) experimental points from References 38 and 169 are calculated from the position of the spin-ordering wave vector]. Filled symbols represent data from momentum-resolved probes (RXS, XRD, neutron scattering), whereas open symbols represent data from real-space methods (STM). Colored lines are guides-to-the-eye; the vertical dashed line marks the location of the doping $p = 0.12$. Abbreviations: Bi2201, $Bi_{2y}Pb_ySr_{2-z}La_zCuO_{6+\delta}$; Bi2212, $Bi_2Sr_2CaCu_2O_{8+\delta}$; Hg1201, $HgBa_2CuO_{4+\delta}$; LBCO, $La_{2-x}Ba_xCuO_{4+\delta}$; LESCO, $La_{2-x-y}Eu_ySr_xCu_2O_{4+\delta}$; Na-CCOC, Na-doped $Ca_2CuO_2Cl_2$; RXS, resonant X-ray scattering; STM, scanning tunneling microscopy; XRD, X-ray diffraction.

between the charge and magnetic instabilities, as previously suggested for the hole-doped cuprates (156–158, 167, 182). Most importantly, and independent of the detailed temperature dependence, the detection of charge order in NCCO conclusively demonstrates that this phenomenon is truly universal in the cuprates, establishing a powerful and robust paradigm for the physics of the lightly doped CuO_2 planes, which transcends the asymmetry inherent to the different orbital character of doped holes (largely on O-2*p* states) versus doped electrons (occupying the Cu-derived upper Hubbard band).

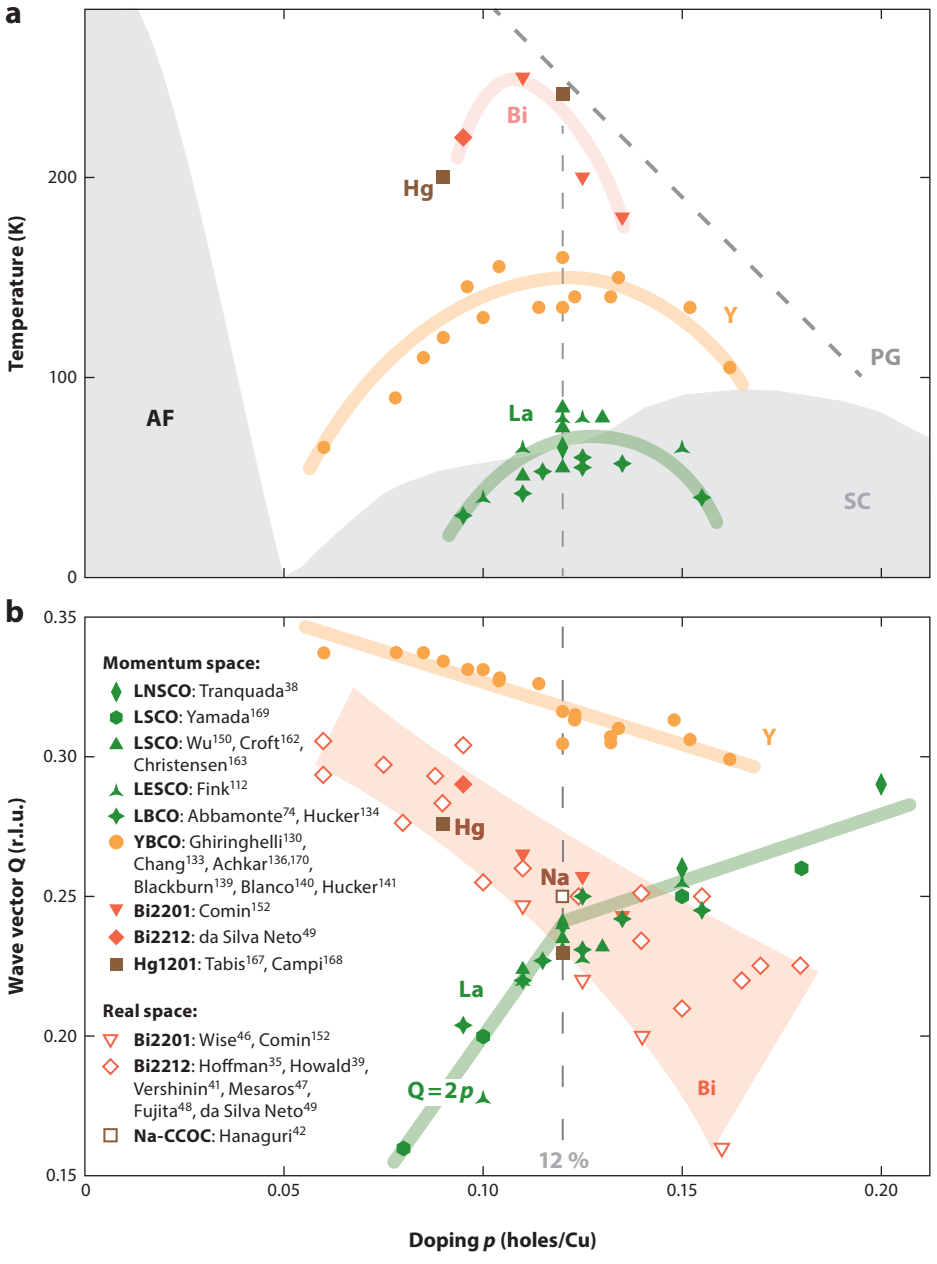

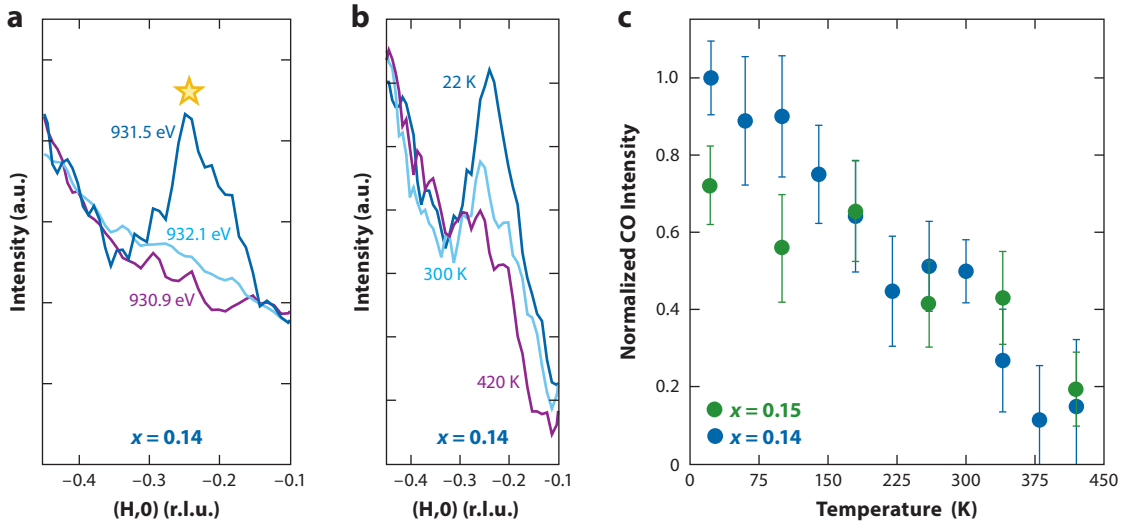

Figure 9

Resonant X-ray scattering (RXS) study of charge order in the electron-doped cuprate $Nd_{2-x}Ce_xCuO_{4+\delta}$ (NCCO). (*a*) Energy- and (*b*) temperature-dependent RXS scans [along (*H*00)] of the charge-order peak around $H \sim 0.25$ r.l.u. in superconducting NCCO with $x = 0.14$. (*c*) Gradual temperature evolution of the charge-order intensity, with a tentative onset temperature around 350–400 K. Adapted from Reference 180 with permission.

3.4. What Hides Behind a Peak: Charge-Order Patterns and Symmetries

As the case for the universality of charge order was receiving increasingly supporting evidence, the theoretical understanding of the origin of this phenomenon and of its interplay with coexisting instabilities, as well as the detailed exploration of the microscopic structure of the ordered state, regained a central role in the context of the physics of copper-based high-temperature superconductors (13, 156–160, 183–187).

In a single-band model charge order would be a scalar field, which can be expressed as the periodic modulation of the occupation of a given electronic orbital as a function of the spatial coordinate. However, the low-energy electronic structure of the CuO_2 planes involves three different orbitals: Cu-3$d_{x^2-y^2}$ (at the copper sites), O-2p_x (at the horizontally bridging oxygen sites), and O-2p_y (at the vertically bridging oxygen sites). Consequently, charge order can be expressed as a vector field with three components (157, 182): (*a*) a site-centered modulation, corresponding to an extra charge residing on the Cu-3*d* orbital (**Figure 10*c***, *top*); (*b*) an extended *s′*-wave bond order, where the spatially modulated density is on the O-2*p* states, and the maxima along the *x* and *y* directions coincide (**Figure 10*c***, *middle*); and (*c*) a *d*-wave bond order, where the charge modulation changes sign between *x*- and *y*-coordinated oxygen atoms, and the maxima are shifted by a half wavelength (**Figure 10*c***, *bottom*). The notation as well as the denomination of "symmetry terms," for the components introduced above, follow from the resulting angular distribution of the phases within the CuO_4 plaquette; this is encoded via an internal momentum variable **k** (restricted to the first Brillouin zone) in addition to the lattice momentum **Q**, in the definition of the charge-order parameter: $\Delta_{CDW}(\mathbf{k}, \mathbf{Q}) = \langle c^{\dagger}_{\mathbf{k}+\mathbf{Q}/2} \cdot c_{\mathbf{k}-\mathbf{Q}/2} \rangle$. This definition enables a full decomposition of the orbital-dependent modulation of the electronic density as a linear combination of the symmetry components introduced above, which therefore serve as a basis set

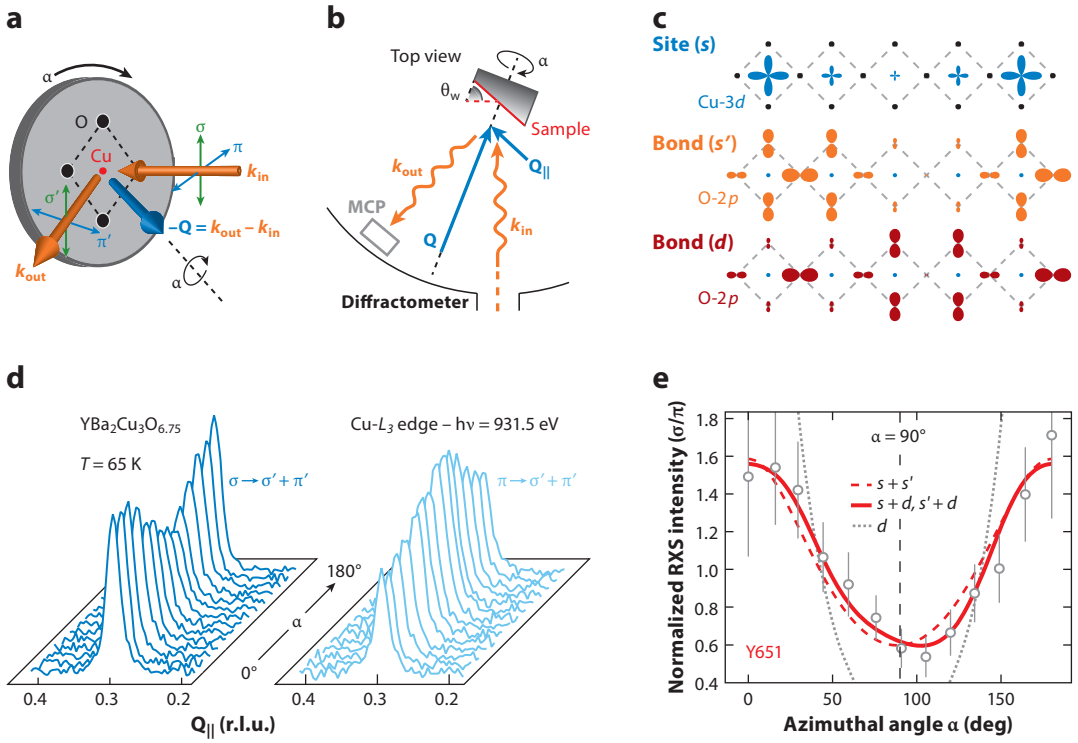

Figure 10

Azimuthal angle-dependent charge scattering and symmetry of charge order in $YBa_2Cu_3O_{6+x}$ (YBCO). (*a*,*b*) Azimuthal geometry for resonant X-ray scattering (RXS) experiments. This allows rotating the crystallographic axes of an angle α around the transferred momentum $\mathbf{Q}$, which is consequently preserved in the frame of reference of the sample. (*c*) Different (but not orthogonal) symmetry representations for the charge-ordered state in a three-orbital system (Cu-3*d*, O-2p_x, and O-2p_y), such as the cuprates. (*d*) The modulation of the RXS signal versus azimuthal angle α is evident from the raw RXS scans across the charge-order peak in underdoped $YBa_2Cu_3O_{6.75}$ for both σ and π polarizations. (*e*) Azimuthal dependence of the ratio of the σ and π charge-order peak intensities, and comparison to the numerical prediction for different binary combinations of the symmetry terms introduced in panel *c*, suggesting a prominent *d*-wave component. Adapted from Reference 188 with permission. Abbreviation: MCP, mobile carrier peak.

for the charge-order parameter, so that the latter can be expressed as (157)

$$\Delta_{\mathrm{CDW}}(\mathbf{k}, \mathbf{Q}) = \Delta_s + \Delta_{s'}(\cos k_x + \cos k_y) + \Delta_d(\cos k_x - \cos k_y), \qquad 15.$$

where Δ_s, $\Delta_{s'}$, and Δ_d represent the magnitude of the *s*-, *s*′-, and *d*-wave terms.

Theoretical predictions in the context of the *t*-*J* model (13, 157, 182, 190) and of the spin-fermion model (156, 159) concluded that a *d*-wave pattern of electronic charges is energetically favored over the other terms. In order to test these theoretical scenarios, an alternative RXS scheme has been recently devised (188, 189) and applied to the study of the local symmetry of charge order in Bi2201 and YBCO (188), and YBCO and LBCO (189). This approach relies on the definition of a local form factor f_{pq} (which is a tensorial quantity; see Equation 9) capable of discriminating between the different symmetry components of charge order. Once the magnitudes of the different components are built into the local form factor [$f_{pq} \rightarrow f_{pq}(\Delta_s, \Delta_{s'}, \Delta_d)$], the scattering yield can be written as

$$I^{\mathrm{RXS}}(\mathbf{Q}) \propto \left| \sum_{pq} (\varepsilon_{v_{\mathrm{in}}})_p \cdot \left[\sum_n f_{pq}^{(n)}(\Delta_s, \Delta_{s'}, \Delta_d) \cdot e^{i\mathbf{Q}\cdot\mathbf{R}_n} \right] \cdot (\varepsilon_{v_{\mathrm{out}}})_q \right|^2, \qquad 16.$$

where $\varepsilon_{v_{in}}$ and $\varepsilon_{v_{out}}$ represent the polarization vectors for incoming and outgoing photons, respectively, while $\mathbf{Q}^*$ is the ordering wave vector. At this point, a single measurement of the RXS intensity will not suffice to resolve the Δ_s, $\Delta_{s'}$, Δ_d terms. This issue is overcome by performing the RXS measurement as a function of the sample rotation around the azimuthal axis (see schematic of experimental geometry in **Figure 10*a,b***), which is collinear with the ordering wave vector. This procedure allows modulating the projection of the form factor onto the light polarization as a function of the azimuthal angle α. Following this approach, the RXS scans can be measured for a range of azimuthal values [see **Figure 10*d*** for the case of YBCO (188)]. The resulting RXS intensities, shown in **Figure 10*e*** for the case of YBCO at the Cu-L_3 edge (188) and in **Figure 11*a,b*** for the case of LBCO at the O-K edge (189), can be fitted to the theoretical model of Equation 16 to evaluate the magnitudes of the symmetry components (which are treated as variational parameters). From these studies, YBCO was concluded to possess a prominent d-wave symmetry (see **Figure 10*e*** and Reference 188), whereas the stripe order in LBCO is best described by an s'-wave pattern (see **Figure 11*c*** and Reference 189). A similar motif was also found in the pattern of atomic displacements in YBCO (146). The determination of the charge-order symmetry in Bi2201 was instead not conclusive using RXS (188). Although these early RXS results are poised to stimulate further work to identify and classify these types of symmetries in momentum space, in a recent STM study of Bi2212 and Na-CCOC, Fujita et al. (191) have successfully implemented the decomposition of Equation 15 by analyzing the reciprocal space representation of the different local symmetries in real space. In particular, these authors first noted how a d-wave [s'-wave] symmetry suppresses the Fourier amplitudes of the $(\pm Q, 0)$ and $(0, \pm Q)$ [$(\pm 1 \pm Q, 0)$, $(0, \pm 1 \pm Q)$, $(\pm 1, \pm Q)$, and $(\pm Q, \pm 1)$] peaks, and subsequently they were able to resolve the extinction of the inner charge-order peaks in reciprocal space starting from the spatially resolved, partial orbital occupation of the O_x, and O_y sites. The detailed analysis of the STM conductance maps finally revealed that charge order in Bi2212 and Na-CCOC also possess a predominant d-wave form factor.

Another key aspect regarding the microscopic description of charge order, and one that has been debated for a long time (7, 12, 185, 192–196), is whether charge order has a checkerboard (bidirectional) or stripe (unidirectional) character. This problem found an early answer in the La-based cuprates, thanks to the coexistence of spin and charge order with a precise wave vector relation that rules out a checkerboard state. However, magnetic and charge order tend to avoid each other in the phase diagram of all other cuprates, a circumstance that, combined with the typical observation of orthogonal [$(Q, 0)$ and $(0, Q)$] charge-order reflections, has hindered a conclusive resolution of the checkerboard/stripe dichotomy. Furthermore, evidence in real space using local probes (STM) has been traditionally hampered by the disorder characterizing Bi-based compounds, which are known to blur the distinction between native uni- and bidirectional ordering instabilities (194, 195); however, recent advancements in the analysis of STM data sets have enabled the visualization of a predominant unidirectional character of electronic modulations in Bi2212 (197).

The first indications of unidirectional charge order in underdoped YBCO came from Blackburn et al. (139) and Blanco-Canosa et al. (140), showing experimental evidence for very unequal amplitudes between the charge-order peak along the **b** axis (strong) and along the **a** axis (weak) in YBCO Ortho-II; this is a direct signature of the tendency toward unidirectional behavior in the charge-order parameter. A recent attempt to assess the character of density modulations was put forth by resolving the full reciprocal space structure of the charge-order peaks in YBCO using RXS (198). The same geometry was used as outlined in **Figure 10*a,b***, which effectively allows slicing through the ordering peak in the (Q_x, Q_y) plane along different directions in reciprocal space. In this study, the line width from the RXS scans (see again **Figure 10*d***) was extracted in

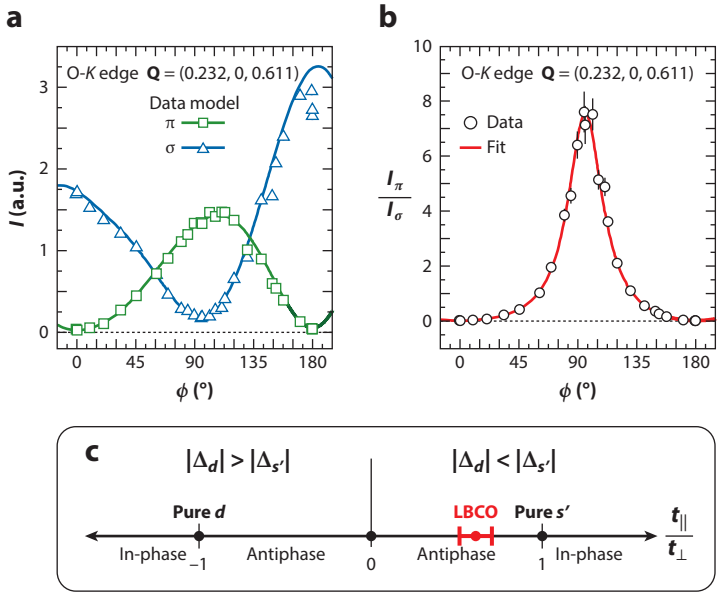

Figure 11

The symmetry of charge order in $La_{2-x}Ba_xCuO_{4+\delta}$ (LBCO). (*a*) Azimuthal dependence of the resonant X-ray scattering (RXS) signal from a stripe-ordered LBCO sample, for the two incoming light polarizations σ and π, with theoretical fit profiles achieving best agreement in the case of predominant s' symmetry. (*b*) Ratio I_π / I_σ of the intensities for the two polarizations and corresponding best fit profile. (*c*) Diagram of the relative weight of s'- and d-wave components as a function of the sign and magnitude of the in-plane ($t_\parallel$) to the out-of-plane ($t_\perp$) X-ray transition amplitudes; the red marker and bar indicates the parameter range yielding the best agreement with the data. Adapted from Reference 189 with permission.

order to reconstruct the two-dimensional peak shape as shown in **Figure 12*a*** for a $YBa_2Cu_3O_{6.51}$ sample. The elongation of the charge-order peaks located along the (100) direction ($\mathbf{Q}_a$) and the (010) direction ($\mathbf{Q}_b$) suggests a locking between the direction of long correlation (narrow peak line width) and the wave vector, occurring for the $YBa_2Cu_3O_{6.51}$ and $YBa_2Cu_3O_{6.67}$ samples, whereas the charge-order peaks in $YBa_2Cu_3O_{6.75}$ exhibit the same elongation. This locking mechanism suggests a breaking of fourfold rotational (D_{4h}) symmetry that is independent for the two ordering components and is, therefore, incompatible with a checkerboard state; the latter, being an equal superposition of density modulations along (100) and (010), imposes the same peak structure for the charge-order peaks $\mathbf{Q}_a$ and $\mathbf{Q}_b$.

The momentum structure of the charge-order peaks already rules out a checkerboard state in favor of a unidirectional (stripy) instability (where stripes can be segregated or overlapping and still generate the same structure in reciprocal space). Further support is provided by the temperature dependence of the longitudinal ($\xi_\parallel$) and transverse ($\xi_\perp$) correlation lengths, which can be derived as the inverse of the peak line width along the direction parallel and perpendicular to the wave vector, respectively; these are shown in **Figure 12*b***. The temperature evolution of the correlation lengths suggests a larger drop, below the SC transition temperature T_c, for the longitudinal (i.e., across the stripes) correlations (see **Figure 12*c***), again leading to a preferential, Q-dependent locking of the density-density correlations and to a breaking of fourfold rotational symmetry.

A similar tendency to a unidirectional character of the charge modulations has also been identified, using RXS, in the different orbital symmetry of the $\mathbf{Q}_a$ and $\mathbf{Q}_b$ peaks (189). This in-plane anisotropy of the short-range charge modulations in YBCO, also detected in NMR measurements

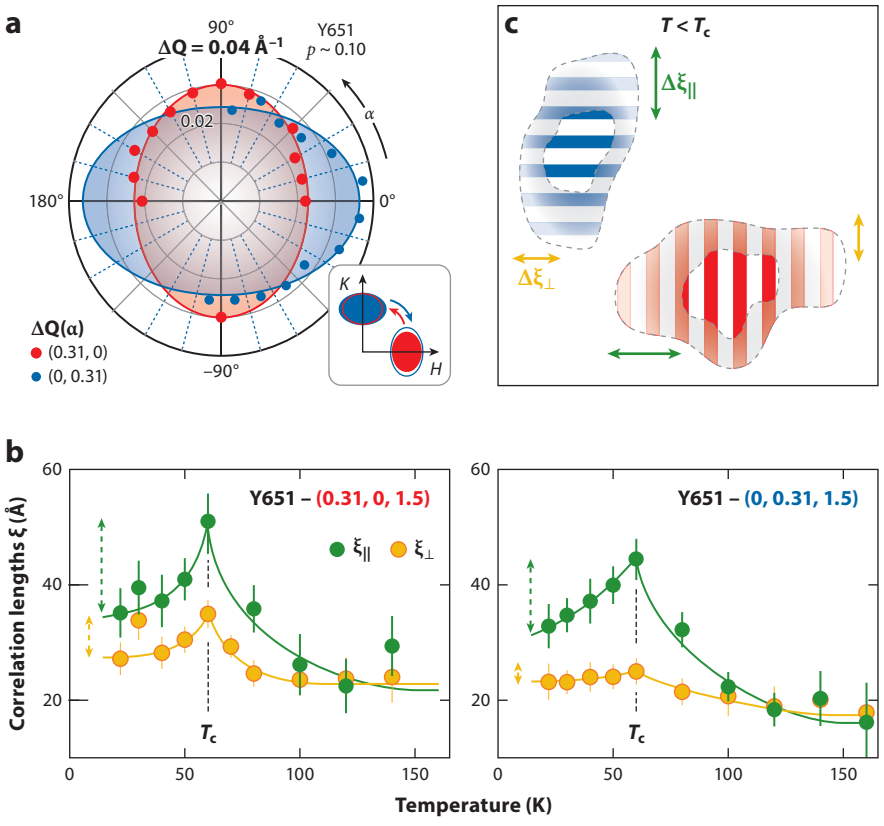

Figure 12

Stripe versus checkerboard symmetry of charge modulations in $YBa_2Cu_3O_{6+x}$ (YBCO). (*a*) Two-dimensional shape of the charge-order peaks at (0.31, 0, 1.5) (*red ellipse*) and (0, 0.31, 1.5) (*blue ellipse*) for a $YBa_2Cu_3O_{6.51}$ sample, as determined from fitting the azimuthal-dependent peak widths (*red* and *blue dots*). (*Bottom-right inset*) Schematic representation of the original peak shapes (*filled ellipses*) and their 90°-rotated versions (*hollow ellipses*). (*b*) Temperature-dependent longitudinal (*green*) and transverse (*yellow*) correlation lengths at (*left*) (0.31, 0, 1.5) and (*right*) (0, 0.31, 1.5), showing a clear anisotropy in the evolution across T_c. (*c*) Illustration of the anisotropy reported in panel *b*, showing how the onset of the superconducting phase reduces the density-density correlations preferentially across the stripes. Adapted from Reference 198 with permission.

(149), have been argued to cause the large in-plane anisotropy of the Nernst signal seen in YBCO near $p = 0.12$ (199), because the Nernst anisotropy grows upon cooling in tandem with the growth in modulation amplitude (200).

4. FUTURE PROSPECTS AND NEW CHALLENGES

Despite the recent flurry of experimental findings and theoretical insights on charge order in the cuprates, there is still a lot to learn and to understand. First and foremost, the mechanism driving the doped holes into breaking translational symmetry has not been conclusively pinned down. In particular, it is unclear whether the cuprates exhibit Peierls physics similar to other low-dimensional compounds (201) or whether a new and unconventional mechanism is at play. Several studies have been performed since the discovery of stripe order aimed at elucidating the

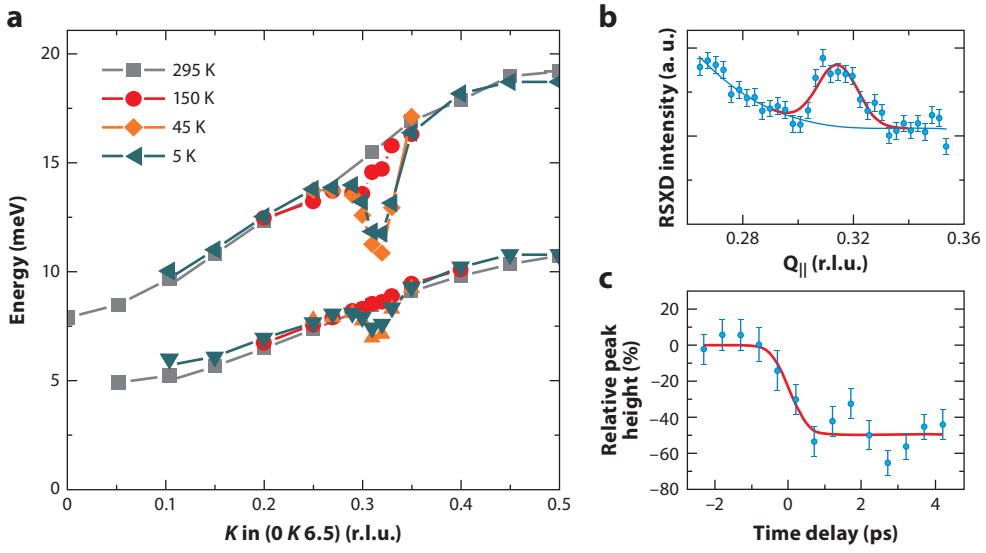

Figure 13

Giant phonon anomaly and charge-order melting from high-resolution frequency- and time-domain X-ray spectroscopy. (*a*) Momentum and temperature dependence of the frequency of low-energy transverse acoustic and optical phonons in underdoped $YBa_2Cu_3O_{6+x}$ (YBCO) ($T_c = 61$ K), showing a sharp softening occurring at the charge-order wave vector $\mathbf{Q}_{CO} = (0, 0.31, 6.5)$ in the superconducting phase ($T < T_c$). Adapted from Reference 144 with permission. (*b*) Charge-order peak in underdoped YBCO ($T_c = 61$ K), acquired using ultrafast soft X-ray pulses from the Linear Coherent Light Source. Abbreviation: RSXD, resonant soft X-ray diffraction. (*c*) Corresponding time-resolved dynamics of the charge-order peak amplitude following impulsive photoexcitation ($t = 0$) of the apical oxygen mode ($\lambda \sim 15\mu$m) using 400-fs pulses. Adapted from Reference 209 with permission.

electron-lattice interplay and its relevance for charge-order instabilities (202–207). Recently, the work by Le Tacon et al. (144) revealed a strong and sharp (in momentum) softening of the low-energy acoustic and optical phonons at the charge-order wave vector in underdoped YBCO [see **Figure 13*a***; similar observations were also made for NCCO (175) and Bi2201 (161)]. This result per se already provides direct evidence of a pronounced electron-lattice coupling mechanism, whereas the partial yet incomplete softening (with the frequency remaining nonzero) further clarifies that the charge order in cuprates is not due to a phonon mode freezing into a static lattice distortion, which is consistent with the short-ranged nature of charge correlations at zero magnetic field. The charge-order peak remains confined to the quasi-elastic line, which bears the typical signatures of a "central peak," and this is characteristic of the presence of ordered nanodomains that gradually coalesce into a state with longer correlations. However, the most puzzling finding emerges from the temperature dependence of the softening effect, which is enhanced in the SC phase, where charge order is paradoxically weakened. This behavior reflects a strong superconductivity-induced phonon anomaly, occurring at the wave vector of the charge instability, thus exposing a very complex intertwining between these competing phases that might deserve further explorations (for a recent theoretical discussion of this phenomenon see Reference 208).

Time-resolved experimental methods, which probe the recovery dynamics of the system following an ultrafast perturbation, have rapidly emerged as an alternative tool to gain further insights on correlated materials. Depending on the nature of the excitation, pump-probe techniques can both probe the microscopic coupling between different degrees of freedom near equilibrium (i.e., in the linear response regime attained at low excitation intensities) (210–213) or explore completely new physics in the strongly perturbative regime (at high excitation intensities) where

photoinduced phases can be probed that are often inaccessible at equilibrium (214). The field of time-resolved scattering and diffraction has seen rapid advancements since its inception at the end of the 1990s (215). New avenues in the X-ray study of ordering phenomena out of equilibrium have been enabled by the recent development of free-electron-laser (FEL) sources, which generate bright ultrashort light pulses over a broad range of energies from the extreme ultraviolet to the hard X-rays, thereby creating new opportunities for the investigation of structural and electron dynamics with high time resolution. The spectral control of the photoexcitation process is an additional experimental parameter, enabling the selective perturbation of specific degrees of freedom via the nonlinear coupling between light and lattice (216, 217). When this framework is combined with photon energy tunability, resonant scattering can be used to probe the recovery of electronic orders that are brought out-of-equilibrium by an ultrafast pump (218, 219). In the context of charge order in the cuprates, these measurements were performed for the first time by Först et al. (209), using ultrafast terahertz light pulses to photoexcite a particular lattice vibration (the apical oxygen mode) in underdoped YBCO and soft X-ray FEL pulses (at the Cu-L_3) to track the evolution of the charge-order peak (**Figure 13*b***) as a function of time. The photoexcitation process strengthens the SC state by promoting coherent interlayer transport, and the charge-order amplitude is correspondingly weakened by a factor of two (see **Figure 13*c***), thus providing new insights on the competition between charge order and superconductivity in a regime where phase coherence is artificially enhanced with light (220, 221) [similar results were also reported in LBCO (222)]. More generally, the new FEL capabilities are poised to considerably extend the domain of application of resonant X-ray methods toward the study of nanoscale ordering phenomena at unprecedented length- and timescales.

Another new frontier for the use of high-brightness X-ray sources is in the context of high-magnetic field studies. The use of high fields within different experimental techniques, such as quantum oscillations or NMR, has been transformative for our understanding of high-temperature superconductors, enabling unprecedented insights into the nature and interplay of competing orders in these complex materials. It was then natural to envisage the extension of high-field capabilities to scattering and diffraction experiments and, notwithstanding the complications caused by the requirement for optical access for incoming and outgoing photon beams, several efforts have been successfully carried forward in this direction in recent years. Chang et al. (133) used a SC cryomagnet specifically designed for low-angle forward-scattering measurements in transmission geometry and using penetrating high-energy photons (100 keV), which enabled the first observation of magnetic field–induced enhancement of the charge-order signal.

Very recently, an innovative experimental scheme was introduced by Gerber et al. (131) that is based on the use of a high-field (28 T) split-pair pulsed magnet synchronized with the ultrabright and ultrafast X-ray pulses (with photon energy of 8.8 keV) of the Linear Coherent Light Source. This approach, leveraging the high single-pulse photon flux of the FEL beam, enabled the acquisition of two-dimensional single-shot diffraction patterns with sufficient photon counts in spite of the very low sampling frequency (with one spectrum every 2 to 25 minutes, due to the recovery time of the pulsed magnetic field apparatus). The corresponding momentum-space maps of charge order in YBCO, from 0 to 25 T, are shown in the upper panels of **Figure 14** and reveal an ostensible evolution in the momentum structure of the charge-order peak as a function of both the in-plane (K) and out-of-plane (L) wave vectors (the latter are plotted also as line cuts in the lower panels of **Figure 14**). In particular, the out-of-plane character of the charge-order peak changes from a very broad, elongated structure at zero field to a well-defined peak (with ∼170 Å correlation length) located around $L = 1$. This is accompanied by a sharpening of the in-plane peak line width, with a corresponding increase of charge correlations from ∼60 to ∼180 Å, and a concomitant enhancement of the diffracted intensity (see **Figure 14*c*,*b***, respectively). These

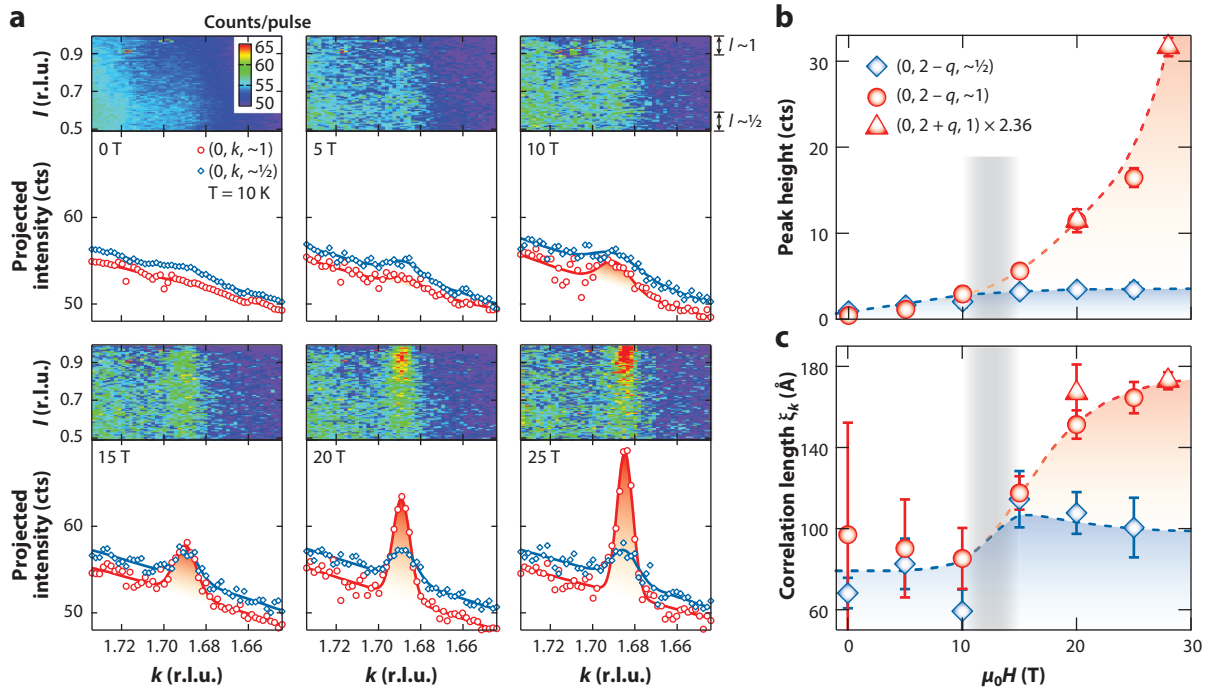

Figure 14

X-ray diffraction from charge order at high magnetic fields. (*a*) Magnetic field–dependent diffraction maps measured on $YBa_2Cu_3O_{6+x}$ using a 8.8-keV photon energy, showing (0*K L*) sections (*top panels*) in momentum space and the corresponding evolution of the charge-order reflection at $\mathbf{Q}_{CO} \sim (0, 2\text{–}0.31, L)$ from 0 to 25 T. Bottom panels show the corresponding line cuts at $L \sim 0.5$ (*blue*) and $L \sim 1$ (*red*) and the evolution of the out-of-plane momentum structure of the charge-order reflection from the zero- to high-field regime. (*b,c*) Peak height and correlation length, respectively, as a function of magnetic field. Adapted from Reference 131 with permission.

results disclose the complexity of charge order and its rich and unconventional phenomenology as a function of doping as well as magnetic field. In particular, this study not only uncovers the momentum-resolved crossover between the low- and high-field regimes, previously investigated using NMR (149), but also clarifies that a full reconstruction of the Fermi surface as seen by quantum oscillations only happens in high field when long-range order sets in, thereby elucidating the absence of folding and small pockets in the ARPES measurements (which can only be performed in zero field) on YBCO (223, 224).

The further development of these novel approaches and methodologies will enable the exploration of completely new dimensions. This will bring us many more surprises and much deeper insights in the study of symmetry breaking instabilities in cuprates and lead to a fuller understanding of these phenomena and their intimate interplay with high-temperature superconductivity.

SUMMARY POINTS

1. **Technical advancements**: The challenge posed by the detection and characterization of charge-density waves in the context of the rich phenomenology of the doped CuO_2 planes

has propelled tremendous advancements in the field of soft X-ray scattering methods. Presently, RXS beamlines are operational or under construction at several facilities worldwide including the following: ALS, APS, BESSY, CLS, DESY, Diamond, ESRF, NSLS-II, NSRRC, SLS, SOLEIL, Spring-8, SSRL.

2. **Universality**: To date, evidence of charge order has been found for all hole-doped cuprate families, as well as in Nd-based electron-doped compounds, using a variety of complementary experimental probes.
3. **Resolution**: RXS has been successfully used to detect charge-density modulations with a spatial coherence as short as 15–20 Å, thus extending to momentum space capabilities that were previously accessible only to spatially resolved techniques (i.e., STM).
4. **Symmetry**: The richness of the RXS information, and the multiple control parameters available—e.g., polarization, photon energy, sample orientation—have opened up the possibility to explore new microscopic aspects of the ordered state, such as its dimensionality (1D versus 2D) and its local symmetry (s-, s'-, and d-wave).

FUTURE DIRECTIONS

1. Unveiling the driving force behind charge order in cuprates.
2. Finding new approaches to modulate and, in general, control charge order.
3. Elucidating the relative role of Mott physics and the proximity to quantum-critical behavior for charge order, as well as superconductivity, in cuprates.
4. Probing the evolution of charge order and its interplay with superconductivity under extreme conditions, such as high magnetic fields, high pressures, and ultrafast optical pumping.

DISCLOSURE STATEMENT

The authors are not aware of any affiliations, memberships, funding, or financial holdings that might be perceived as affecting the objectivity of this review.

ACKNOWLEDGMENTS

The authors are indebted to P. Abbamonte, L. Braicovich, A. Cavalleri, E.H. da Silva Neto, J.C. Davis, J. Fink, J. Geck, G. Ghiringhelli, C. Giannetti, R.L. Greene, M. Greven, D.G. Hawthorn, F. He, J.E. Hoffman, M.-H. Julien, B. Keimer, S.A. Kivelson, M. Le Tacon, P.A. Lee, W.S. Lee, C. Mazzoli, M.R. Norman, S. Sachdev, G.A. Sawatzky, E. Schierle, R. Sutarto, L. Taillefer, J.M. Tranquada, E. Weschke, and S. Wilkins for valuable discussions and for the critical reading of this review.

This work was supported by the Max Planck-UBC Centre for Quantum Materials; the Killam, A.P. Sloan, A. von Humboldt Foundations' and NSERC's Steacie Memorial Fellowships (A.D.); the Canada Research Chairs Program (A.D.); NSERC; CFI; and CIFAR Quantum Materials.

LITERATURE CITED

1. Dagotto E. 2005. *Science* 309:257–62
2. Norman MR. 2011. *Science* 332:196–200
3. Zaanen J, Sawatzky GA, Allen JW. 1985. *Phys. Rev. Lett.* 55:418–21
4. Lee PA, Nagaosa N, Wen XG. 2006. *Rev. Mod. Phys.* 78:17–85
5. Bednorz JG, Müller KA. 1986. *Zeit. Phys. B* 64:189–93
6. Emery VJ, Kivelson SA, Tranquada JM. 1999. *PNAS* 96:8814–17
7. Kivelson SA, Bindloss IP, Fradkin E, Oganesyan V, Tranquada JM, et al. 2003. *Rev. Mod. Phys.* 75:1201–41
8. Sachdev S, Demler E. 2004. *Phys. Rev. B* 69:144504
9. Birgeneau RJ, Stock C, Tranquada JM, Yamada K. 2006. *J. Phys. Soc. Jpn.* 75:111003
10. Varma CM. 2006. *Phys. Rev. B* 73:155113
11. Li Y, Baledent V, Barisic N, Cho Y, Fauque B, et al. 2008. *Nature* 455:372–75
12. Berg E, Fradkin E, Kivelson S, Tranquada J. 2009. *N. J. Phys.* 11:115004
13. Davis JCS, Lee DH. 2013. *PNAS* 110:17623
14. Fradkin E, Kivelson SA, Tranquada JM. 2015. *Rev. Mod. Phys.* 87:457–82
15. Tranquada JM, Moudden AH, Goldman AI, Zolliker P, Cox DE, et al. 1988. *Phys. Rev. B* 38:2477–85
16. Birgeneau RJ, Gabbe DR, Jenssen HP, Kastner MA, Picone PJ, et al. 1988. *Phys. Rev. B* 38:6614–23
17. Yoshizawa H, Mitsuda S, Kitazawa H, Katsumata K. 1988. *J. Phys. Soc. Jpn.* 57:3686–89
18. Birgeneau RJ, Endoh Y, Kakurai K, Hidaka Y, Murakami T, et al. 1989. *Phys. Rev. B* 39:2868–71
19. Thurston TR, Birgeneau RJ, Kastner MA, Preyer NW, Shirane G, et al. 1989. *Phys. Rev. B* 40:4585–95
20. Fujita M, Yamada K, Hiraka H, Gehring PM, Lee SH, et al. 2002. *Phys. Rev. B* 65:064505
21. Cheong SW, Aeppli G, Mason TE, Mook H, Hayden SM, et al. 1991. *Phys. Rev. Lett.* 67:1791–94
22. Schrieffer JR, Wen XG, Zhang SC. 1988. *Phys. Rev. Lett.* 60:944–47
23. Machida K. 1989. *Phys. C: Supercond.* 158:192–96
24. Castellani C, Di Castro C, Grilli M. 1995. *Phys. Rev. Lett.* 75:4650–53
25. Zaanen J, Gunnarsson O. 1989. *Phys. Rev. B* 40:7391
26. Poilblanc D, Rice TM. 1989. *Phys. Rev. B* 39:9749–52
27. Schulz HJ. 1990. *Phys. Rev. Lett.* 64:1445–48
28. Emery VJ, Kivelson SA, Lin HQ. 1990. *Phys. Rev. Lett.* 64:475–78
29. Tranquada JM, Buttrey DJ, Sachan V, Lorenzo JE. 1994. *Phys. Rev. Lett.* 73:1003–6
30. Tranquada JM, Sternlieb BJ, Axe JD, Nakamura Y, Uchida S. 1995. *Nature* 375:561–63
31. Tranquada JM, Axe JD, Ichikawa N, Nakamura Y, Uchida S, Nachumi B. 1996. *Phys. Rev. B* 54:7489–99
32. Fujita M, Goka H, Yamada K, Matsuda M. 2002. *Phys. Rev. Lett.* 88:167008
33. v. Zimmermann M, Vigliante A, Niemller T, Ichikawa N, Frello T, et al. 1998. *Europhys. Lett.* 41:629
34. Kastner MA, Birgeneau RJ, Shirane G, Endoh Y. 1998. *Rev. Mod. Phys.* 70:897–928
35. Hoffman JE, Hudson EW, Lang KM, Madhavan V, Eisaki H, et al. 2002. *Science* 295:466–69
36. Chen HD, Hu JP, Capponi S, Arrigoni E, Zhang SC. 2002. *Phys. Rev. Lett.* 89:137004
37. Lake B, Aeppli G, Clausen KN, McMorrow DF, Lefmann K, et al. 2001. *Science* 291:1759–62
38. Tranquada JM, Axe JD, Ichikawa N, Moodenbaugh AR, Nakamura Y, Uchida S. 1997. *Phys. Rev. Lett.* 78:338–41
39. Howald C, Eisaki H, Kaneko N, Kapitulnik A. 2003. *PNAS* 100:9705–9
40. Hoffman JE, McElroy K, Lee DH, Lang KM, Eisaki H, et al. 2002. *Science* 297:1148–51
41. Vershinin M, Misra S, Ono S, Abe Y, Ando Y, Yazdani A. 2004. *Science* 303:1995–98
42. Hanaguri T, Lupien C, Kohsaka Y, Lee DH, Azuma M, et al. 2004. *Nature* 430:1001–5
43. Kohsaka Y, Taylor C, Fujita K, Schmidt A, Lupien C, et al. 2007. *Science* 315:1380–85
44. Kohsaka Y, Taylor C, Wahl P, Schmidt A, Lee J, et al. 2008. *Nature* 454:1072–78
45. Lee J, Fujita K, Schmidt AR, Kim CK, Eisaki H, et al. 2009. *Science* 325:1099–103
46. Wise WD, Boyer MC, Chatterjee K, Kondo T, Takeuchi T, et al. 2008. *Nat. Phys.* 4:696–99
47. Mesaros A, Fujita K, Eisaki H, Uchida S, Davis JC, et al. 2011. *Science* 333:426–30
48. Fujita K, Schmidt AR, Kim EA, Lawler MJ, Lee DH, et al. 2012. *J. Phys. Soc. Jpn.* 81:011005
49. da Silva Neto E, Aynajian P, Frano A, Comin R, Schierle E, et al. 2014. *Science* 343:393–96

50. Parker CV, Aynajian P, da Silva Neto EH, Pushp A, Ono S, et al. 2010. *Nature* 468:677–80
51. da Silva Neto EH, Parker CV, Aynajian P, Pushp A, Yazdani A, et al. 2012. *Phys. Rev. B* 85:104521
52. He Y, Yin Y, Zech M, Soumyanarayanan A, Yee MM, et al. 2014. *Science* 344:608–11
53. Peli S, Dal Conte S, Comin R, Nembrini N, Banfi F, et al. 2015. arXiv:1508.0307
54. Fujita K, Kim CK, Lee I, Lee J, Hamidian MH, et al. 2014. *Science* 344:612–16
55. Fischer O, Kugler M, Maggio-Aprile I, Berthod C, Renner C. 2007. *Rev. Mod. Phys.* 79:353–419
56. Fujita K, Hamidian M, Firmo I, Mukhopadhyay S, Kim CK, et al. 2015. In *Strongly Correlated Systems*, ed. A Avella, F Mancini, pp. 73–110. Heidelberg: Springer
57. Yazdani A, da Silva Neto EH, Aynajian P. 2016. *Annu. Rev. Condens. Matter Phys.* 7:11–33
58. Als-Nielsen J, McMorrow D. 2011. *Elements of Modern X-Ray Physics*, 2nd ed. Wiley
59. Hendrickson WA. 2014. *Q. Rev. Biophys.* 47:49–93
60. de Bergevin F, Brunel M. 1972. *Phys. Lett. A* 39:141–42
61. Platzman PM, Tzoar N. 1970. *Phys. Rev. B* 2:3556–59
62. Brunel M, de Bergevin F. 1981. *Acta Cryst. A* 37:324–31
63. Gibbs D, Moncton DE, D'Amico KL, Bohr J, Grier BH. 1985. *Phys. Rev. Lett.* 55:234–37
64. Brunel M, de Bergevin F. 1985. *J. Phys. Soc. Jpn.* 54:4099–102
65. Gibbs D, Bohr J, Axe JD, Moncton DE, D'Amico KL. 1986. *Phys. Rev. B* 34:8182–85
66. Bohr J, Gibbs D, Moncton D, D'Amico KL. 1986. *Phys. A: Stat. Mech. Appl.* 140:349–58
67. Goldman AI, Mohanty K, Shirane G, Horn PM, Greene RL, et al. 1987. *Phys. Rev. B* 36:5609–12
68. Blume M. 1985. *J. Appl. Phys.* 57:3615–18
69. Blume M, Gibbs D. 1988. *Phys. Rev. B* 37:1779–89
70. Hannon JP, Trammell GT, Blume M, Gibbs D. 1988. *Phys. Rev. Lett.* 61:1245–48
71. Materlik G, Sparks CJ. 1994. *Resonant Anomalous X-Ray Scattering: Theory and Applications*. Amsterdam: North-Holland
72. Carra P, Thole BT. 1994. *Rev. Mod. Phys.* 66:1509–15
73. Abbamonte P, Blumberg G, Rusydi A, Gozar A, Evans PG, et al. 2004. *Nature* 431:1078–81
74. Abbamonte P, Rusydi A, Smadici S, Gu GD, Sawatzky GA, Feng DL. 2005. *Nat. Phys.* 1:155–58
75. Mariot JM, Karnatak R, Bonnelle C. 1974. *J. Phys. Chem. Solids* 35:657–61
76. Bonnelle C, Karnatak RC, Spector N. 1977. *J. Phys. B: Atomic Mol. Phys.* 10:795
77. Karnatak RC, Esteva JM, Connerade JP. 1981. *J. Phys. B: Atomic Mol. Phys.* 14:4747
78. van der Laan G, Thole BT, Sawatzky GA, Goedkoop JB, Fuggle JC, et al. 1986. *Phys. Rev. B* 34:6529–31
79. Thole BT, van der Laan G, Fuggle JC, Sawatzky GA, Karnatak RC, Esteva JM. 1985. *Phys. Rev. B* 32:5107–18
80. Kuiper P, Kruizinga G, Ghijsen J, Grioni M, Weijs PJW, et al. 1988. *Phys. Rev. B* 38:6483–89
81. de Groot FMF, Grioni M, Fuggle JC, Ghijsen J, Sawatzky GA, Petersen H. 1989. *Phys. Rev. B* 40:5715–23
82. Tröger L, Arvanitis D, Rabus H, Wenzel L, Baberschke K. 1990. *Phys. Rev. B* 41:7297–300
83. Krol A, Lin CS, Ming ZH, Sher CJ, Kao YH, et al. 1990. *Phys. Rev. B* 42:2635–38
84. Jark W, Stöhr J. 1988. *Nucl. Instrum. Methods A* 266:654–58
85. Kao C, Hastings JB, Johnson ED, Siddons DP, Smith GC, Prinz GA. 1990. *Phys. Rev. Lett.* 65:373–76
86. Rusydi A. 2006. *Resonant soft X-ray scattering and charge density waves in correlated systems*. PhD Thesis, University of Groningen, The Netherlands
87. Tonnerre JM, Sève L, Raoux D, Soullié G, Rodmacq B, Wolfers P. 1995. *Phys. Rev. Lett.* 75:740–43
88. MacKay JF, Teichert C, Savage DE, Lagally MG. 1996. *Phys. Rev. Lett.* 77:3925–28
89. Drr HA, Dudzik E, Dhesi SS, Goedkoop JB, van der Laan G, et al. 1999. *Science* 284:2166–68
90. Roper M, van der Laan G, Drr H, Dudzik E, Collins S, et al. 2001. *Nucl. Instrum. Methods A: Accelerators, Spectrometers, Detectors and Associated Equipment* 467–68, Part 2:1101–4
91. Wilkins SB, Hatton PD, Roper MD, Prabhakaran D, Boothroyd AT. 2003. *Phys. Rev. Lett.* 90:187201
92. Wilkins SB, Spencer PD, Hatton PD, Collins SP, Roper MD, et al. 2003. *Phys. Rev. Lett.* 91:167205
93. Grabis J, Nefedov A, Zabel H. 2003. *Rev. Sci. Instrum.* 74:4048
94. Staub U, Scagnoli V, Mulders AM, Katsumata K, Honda Z, et al. 2005. *Phys. Rev. B* 71:214421
95. Hawthorn DG, He F, Venema L, Davis H, Achkar AJ, et al. 2011. *Rev. Sci. Instrum.* 82:073104
96. Hill JP, Kao CC, Caliebe WAL, Matsubara M, Kotani A, et al. 1998. *Phys. Rev. Lett.* 80:4967–70
97. Abbamonte P, Burns CA, Isaacs ED, Platzman PM, Miller LL, et al. 1999. *Phys. Rev. Lett.* 83:860–63

98. Hasan MZ, Isaacs ED, Shen ZX, Miller LL, Tsutsui K, et al. 2000 288:1811–14
99. Kim YJ, Hill JP, Burns CA, Wakimoto S, Birgeneau RJ, et al. 2002. *Phys. Rev. Lett.* 89:177003
100. Abbamonte P, Venema L, Rusydi A, Sawatzky GA, Logvenov G, Bozovic I. 2002. *Science* 297:581–84
101. Nücker N, Fink J, Fuggle JC, Durham PJ, Temmerman WM. 1988. *Phys. Rev. B* 37:5158–63
102. Romberg H, Alexander M, Nücker N, Adelmann P, Fink J. 1990. *Phys. Rev. B* 42:8768–71
103. Chen CT, Tjeng LH, Kwo J, Kao HL, Rudolf P, et al. 1992. *Phys. Rev. Lett.* 68:2543
104. Fink J, Schierle E, Weschke E, Geck J. 2013. *Rep. Progress Phys.* 76:056502
105. Di Matteo S. 2012. *J. Phys. D: Appl. Phys.* 45:163001
106. Bruus H, Flensberg K. 2004. *Many-Body Quantum Theory in Condensed Matter Physics: An Introduction*. Oxford, UK: Oxford Univ. Press
107. Schüßler-Langeheine C, Schlappa J, Tanaka A, Hu Z, Chang CF, et al. 2005. *Phys. Rev. Lett.* 95:156402
108. Dhesi SS, Mirone A, De Nadaï C, Ohresser P, Bencok P, et al. 2004. *Phys. Rev. Lett.* 92:056403
109. Thomas KJ, Hill JP, Grenier S, Kim YJ, Abbamonte P, et al. 2004. *Phys. Rev. Lett.* 92:237204
110. Wilkins SB, Dean MPM, Fink J, Hücker M, Geck J, et al. 2011. *Phys. Rev. B* 84:195101
111. Hücker M, v. Zimmermann M, Gu GD, Xu ZJ, Wen JS, et al. 2011. *Phys. Rev. B* 83:104506
112. Fink J, Schierle E, Weschke E, Geck J, Hawthorn D, et al. 2009. *Phys. Rev. B* 79:100502
113. Fink J, Soltwisch V, Geck J, Schierle E, Weschke E, Büchner B. 2011. *Phys. Rev. B* 83:092503
114. McElroy K, Hoffman JE, Lee DH, Lang KM, Eisaki H, et al. 2003. *Physica C* 388-389:225–26
115. Hoffman JE, Hudson EW, Lang KM, Eisaki H, Uchida S, Davis JC. 2003. *Physica C* 388-389:703–4
116. Howald C, Eisaki H, Kaneko N, Greven M, Kapitulnik A. 2003. *Phys. Rev. B* 67:014533
117. McElroy K, Lee DH, Hoffman JE, Lang KM, Lee J, et al. 2005. *Phys. Rev. Lett.* 94:197005
118. da Silva Neto EH, Aynajian P, Parker CV, Yazdani A. 2012. *Phys. C: Supercond.* 481:153–60
119. Fujita K, Schmidt AR, Kim EA, Lawler MJ, Lee DH, et al. 2012. *J. Phys. Soc. Jpn.* 81:011005
120. Liang R, Bonn D, Hardy WN. 2000. *Phys. C: Supercond.* 336:57–62
121. Doiron-Leyraud N, Proust C, LeBoeuf D, Levallois J, Bonnemaison JB, et al. 2007. *Nature* 447:565–68
122. LeBoeuf D, Doiron-Leyraud N, Levallois J, Daou R, Bonnemaison JB, et al. 2007. *Nature* 450:533–36
123. Hussey NE, Abdel-Jawad M, Carrington A, Mackenzie AP, Balicas L. 2003. *Nature* 425:814–17
124. Platé M, Mottershead JDF, Elfimov IS, Peets DC, Liang R, et al. 2005. *Phys. Rev. Lett.* 95:077001
125. Taillefer L. 2009. *J. Phys.: Condens. Matter* 21:164212
126. Chang J, Daou R, Proust C, LeBoeuf D, Doiron-Leyraud N, et al. 2010. *Phys. Rev. Lett.* 104:057005
127. Laliberté F, Chang J, Doiron-Leyraud N, Hassinger E, Daou R, et al. 2011. *Nat. Commun.* 2:432
128. Wu T, Mayaffre H, Kramer S, Horvatic M, Berthier C, et al. 2011. *Nature* 477:191–94
129. Hawthorn DG, Shen KM, Geck J, Peets DC, Wadati H, et al. 2011. *Phys. Rev. B* 84:075125
130. Ghiringhelli G, Le Tacon M, Minola M, Blanco-Canosa S, Mazzoli C, et al. 2012. *Science* 337:821–25
131. Gerber S, Jang H, Nojiri H, Matsuzawa S, Yasumura H, et al. 2015. arXiv:1506.07910
132. Blanco-Canosa S, Frano A, Schierle E, Porras J, Loew T, et al. 2014. *Phys. Rev. B* 90:054513
133. Chang J, Blackburn E, Holmes AT, Christensen NB, Larsen J, et al. 2012. *Nat. Phys.* 8:871–76
134. Hücker M, v. Zimmermann M, Xu ZJ, Wen JS, Gu GD, Tranquada JM. 2013. *Phys. Rev. B* 87:014501
135. Achkar AJ, He F, Sutarto R, Geck J, Zhang H, et al. 2013. *Phys. Rev. Lett.* 110:017001
136. Achkar AJ, Sutarto R, Mao X, He F, Frano A, et al. 2012. *Phys. Rev. Lett.* 109:167001
137. Benjamin D, Abanin D, Abbamonte P, Demler E. 2013. *Phys. Rev. Lett.* 110:137002
138. Thampy V, Blanco-Canosa S, Garcia-Fernandez M, Dean MPM, Gu GD, et al. 2013. *Phys. Rev. B* 88:024505
139. Blackburn E, Chang J, Hücker M, Holmes AT, Christensen NB, et al. 2013. *Phys. Rev. Lett.* 110:137004
140. Blanco-Canosa S, Frano A, Loew T, Lu Y, Porras J, et al. 2013. *Phys. Rev. Lett.* 110:187001
141. Hücker M, Christensen NB, Holmes AT, Blackburn E, Forgan EM, et al. 2014. *Phys. Rev. B* 90:054514
142. Achkar AJ, Mao X, McMahon C, Sutarto R, He F, et al. 2014. *Phys. Rev. Lett.* 113:107002
143. Bakr M, Souliou SM, Blanco-Canosa S, Zegkinoglou I, Gretarsson H, et al. 2013. *Phys. Rev. B* 88:214517
144. Le Tacon M, Bosak A, Souliou SM, Dellea G, Loew T, et al. 2014. *Nat. Phys.* 10:52–58
145. Blackburn E, Chang J, Said AH, Leu BM, Liang R, et al. 2013. *Phys. Rev. B* 88:054506
146. Forgan EM, Blackburn E, Holmes AT, Briffa AKR, Chang J, et al. 2015. *Nat. Comm.* 6:10064
147. Wu T, Mayaffre H, Kramer S, Horvatic M, Berthier C, et al. 2013. *Nat. Comm.* 4:2113
148. LeBoeuf D, Kramer S, Hardy WN, Liang R, Bonn DA, Proust C. 2013. *Nat. Phys.* 9:79–83

149. Wu T, Mayaffre H, Kramer S, Horvatic M, Berthier C, et al. 2015. *Nat. Comm.* 6:6438
150. Wu HH, Buchholz M, Trabant C, Chang C, Komarek A, et al. 2012. *Nat. Comm.* 3:1023
151. Rosen J, Comin R, Levy G, Fournier D, Zhu ZH, et al. 2013. *Nat. Commun.* 4:1977
152. Comin R, Frano A, Yee M, Yoshida Y, Eisaki H, et al. 2014. *Science* 343:390–92
153. Hashimoto M, Ghiringhelli G, Lee WS, Dellea G, Amorese A, et al. 2014. *Phys. Rev. B* 89:220511
154. Kawasaki S, Lin C, Kuhns PL, Reyes AP, Zheng G-q. 2010. *Phys. Rev. Lett.* 105:137002
155. Shen KM, Ronning F, Lu DH, Baumberger F, Ingle NJC, et al. 2005. *Science* 307:901–4
156. Efetov KB, Meier H, Pépin C. 2013. *Nat. Phys.* 9:442
157. Sachdev S, La Placa R. 2013. *Phys. Rev. Lett.* 111:027202
158. Meier H, Einenkel M, Pépin C, Efetov KB. 2013. *Phys. Rev. B* 88:020506
159. Wang Y, Chubukov A. 2014. *Phys. Rev. B* 90:035149
160. Lee PA. 2014. *Phys. Rev. X* 4:031017
161. Bonnoit C, Gardner D, Chisnell R, Said A, Okada Y, et al. 2012. arXiv:1202.4994
162. Croft TP, Lester C, Senn MS, Bombardi A, Hayden SM. 2014. *Phys. Rev. B* 89:224513
163. Christensen NB, Chang J, Larsen J, Fujita M, Oda M, et al. 2014. arXiv:1404.3192
164. Thampy V, Dean MPM, Christensen NB, Steinke L, Islam Z, et al. 2014. *Phys. Rev. B* 90:100510
165. Doiron-Leyraud N, Lepault S, Cyr-Choinière O, Vignolle B, Grissonnanche G, et al. 2013. *Phys. Rev. X* 3:021019
166. Barisic N, Badoux S, Chan MK, Dorow C, Tabis W, et al. 2013. *Nat. Phys.* 9:761–64
167. Tabis W, Li Y, Le Tacon M, Braicovich L, Kreyssig A, et al. 2014. *Nat. Comm.* 5:5875
168. Campi G, Bianconi A, Poccia N, Bianconi G, Barba L, et al. 2015. *Nature* 525: 359–62
169. Yamada K, Lee CH, Kurahashi K, Wada J, Wakimoto S, et al. 1998. *Phys. Rev. B* 57:6165–72
170. Achkar A. 2015. *Charge density wave order in cuprate superconductors studied by resonant soft X-ray scattering*. PhD Thesis. University of Waterloo, Canada
171. Sebastian SE, Harrison N, Lonzarich GG. 2012. *Rep. Prog. Phys.* 75:102501
172. Ramshaw BJ, Sebastian SE, McDonald RD, Day J, Tan BS, et al. 2015. *Science* 348:317–20
173. Chubukov AV, Sachdev S, Ye J. 1994. *Phys. Rev. B* 49:11919–61
174. Sachdev S. 2000. *Science* 288:475–80
175. d'Astuto M, Mang PK, Giura P, Shukla A, Ghigna P, et al. 2002. *Phys. Rev. Lett.* 88:167002
176. Helm T, Kartsovnik MV, Bartkowiak M, Bittner N, Lambacher M, et al. 2009. *Phys. Rev. Lett.* 103:157002
177. Hinton JP, Koralek JD, Yu G, Motoyama EM, Lu YM, et al. 2013. *Phys. Rev. Lett.* 110:217002
178. Lee WS, Lee JJ, Nowadnick EA, Gerber S, Tabis W, et al. 2014. *Nat. Phys.* 10:883–89
179. Ishii K, Fujita M, Sasaki T, Minola M, Dellea G, et al. 2014. *Nat. Comm.* 5:3714
180. da Silva Neto EH, Comin R, He F, Sutarto R, Jiang Y, et al. 2015. *Science* 347:282–85
181. Motoyama EM, Yu G, Vishik IM, Vajk OP, Mang PK, Greven M. 2007. *Nature* 445:186
182. Metlitski MA, Sachdev S. 2010. *Phys. Rev. B* 82:075128
183. He Y, Scherpelz P, Levin K. 2013. *Phys. Rev. B* 88:064516
184. Bulut S, Atkinson WA, Kampf AP. 2013. *Phys. Rev. B* 88:155132
185. Nie L, Tarjus G, Kivelson SA. 2014. *PNAS* 111:7980–85
186. Dalla Torre EG, He Y, Benjamin D, Demler E. 2015. *N. J. Phys.* 111:022001
187. Melikyan A, Norman MR. 2014. *Phys. Rev. B* 89:024507
188. Comin R, Sutarto R, He F, da Silva Neto EH, Chauviere L, et al. 2015. *Nat. Mater.* 14:796–800
189. Achkar AJ, He F, Sutarto R, McMahon C, Zwiebler M, et al. 2014. arXiv:1409.6787
190. Vojta M, Rösch O. 2008. *Phys. Rev. B* 77:094504
191. Fujita K, Hamidian MH, Edkins SD, Kim CK, Kohsaka Y, et al. 2014. *PNAS* 111:E3026–32
192. Kivelson SA, Fradkin E, Emery VJ. 1998. *Nature* 393:550–53
193. Norman M. 2004. *Science* 303:1985–86
194. Del Maestro A, Rosenow B, Sachdev S. 2006. *Phys. Rev. B* 74:024520
195. Robertson JA, Kivelson SA, Fradkin E, Fang AC, Kapitulnik A. 2006. *Phys. Rev. B* 74:134507
196. Vojta M. 2012. *Phys. C: Supercond.* 481:178–88
197. Hamidian MH, Edkins SD, Kim CK, Davis JC, Mackenzie AP, et al. 2015. arXiv:1507.07865
198. Comin R, Sutarto R, da Silva Neto EH, Chauviere L, Liang R, et al. 2015. *Science* 347:1335–39
199. Daou R, Chang J, LeBoeuf D, Cyr-Choiniere O, Laliberte F, et al. 2010. *Nature* 463:519–22

200. Cyr-Choinière O, Grissonnanche G, Badoux S, Day J, Bonn DA, et al. 2015. arXiv:1504.06972
201. Grüner G. 1994. *Density Waves in Solids*. Boulder, CO: Westview
202. Reznik D, Pintschovius L, Ito M, Iikubo S, Sato M, et al. 2006. *Nature* 440:1170–73
203. Reznik D, Pintschovius L, Fujita M, Yamada K, Gu G, Tranquada J. 2007. *J. Low Temp. Phys.* 147:353–64
204. Reznik D, Pintschovius L, Tranquada JM, Arai M, Endoh Y, et al. 2008. *Phys. Rev. B* 78:094507
205. Reznik D. 2010. *Adv. Condens. Matter Phys.* 2010:523549
206. Raichle M, Reznik D, Lamago D, Heid R, Li Y, et al. 2011. *Phys. Rev. Lett.* 107:177004
207. Reznik D. 2012. *Phys. C: Supercond.* 481:75–92
208. Liu YH, Konik RM, Rice TM, Zhang FC. 2015. arXiv:1506.01258
209. Först M, Frano A, Kaiser S, Mankowsky R, Hunt CR, et al. 2014. *Phys. Rev. B* 90:184514
210. Orenstein J. 2012. *Phys. Today* 65:44–50
211. Dal Conte S, Giannetti C, Coslovich G, Cilento F, Bossini D, et al. 2012. *Science* 335:1600–3
212. Torchinsky DH, Mahmood F, Bollinger AT, Ivan Bozovic I, Gedik N. 2013. *Nat. Mater.* 12:387–91
213. Hinton JP, Koralek JD, Lu YM, Vishwanath A, Orenstein J, et al. 2013. *Phys. Rev. B* 88:060508
214. Fausti D, Tobey RI, Dean N, Kaiser S, Dienst A, et al. 2011. *Science* 331:189–91
215. Rose-Petruck C, Jimenez R, Guo T, Cavalleri A, Siders CW, et al. 1999. *Nature* 398:310–12
216. Först M, Manzoni C, Kaiser S, Tomioka Y, Tokura Y, et al. 2011. *Nat. Phys.* 7:854–56
217. Mankowsky R, Subedi A, Först M, Mariager SO, Chollet M, et al. 2014. *Nature* 516:71–73
218. Först M, Tobey RI, Wall S, Bromberger H, Khanna V, et al. 2011. *Phys. Rev. B* 84:241104(R)
219. Caviglia AD, Först M, Scherwitzl R, Khanna V, Bromberger H, et al. 2013. *Phys. Rev. B* 88:220401
220. Kaiser S, Hunt CR, Nicoletti D, Hu W, Gierz I, et al. 2014. *Phys. Rev. B* 89:184516
221. Hu W, Kaiser S, Nicoletti D, Hunt C, Gierz I, Hoffmann MC, et al. 2014. *Nat. Mater.* 13:705
222. Först M, Tobey RI, Bromberger H, Wilkins SB, Khanna V, et al. 2014. *Phys. Rev. Lett.* 112:157002
223. Hossain MA, Mottershead JDF, Fournier D, Bostwick A, McChesney JL, et al. 2008. *Nat. Phys.* 4:527–31
224. Fournier D, Levy G, Pennec Y, McChesney JL, Bostwick A, et al. 2010. *Nat. Phys.* 6:905–11

Annual Review
of Condensed
Matter Physics

Volume 7, 2016

Contents

Errata

An online log of corrections to *Annual Review of Condensed Matter Physics* articles may be found at http://www.annualreviews.org/errata/conmatphys